Supplementary Materials for

Weakly solvating aqueous-based electrolyte facilitated by a soft co-solvent for extreme temperature operations of zinc-ion batteries

Ruizhi Zhang [a,b,c], Wei Kong Pang [b], Jitraporn (Pimm) Vongsvivut [d], Jodie A. Yuwono [a], Guanjie Li [a], Yanqiu Lyu [a], Yameng Fan [b], Yunlong Zhao [e], Shilin Zhang [a], Jianfeng Mao [a], Qiong Cai [c*], Sailin Liu [a*] and Zaiping Guo [a*]

a School of Chemical Engineering, The University of Adelaide; Adelaide, SA 5005, Australia.
b Institute for Superconducting & Electronic Materials, University of Wollongong; Wollongong, NSW 2500, Australia.
c School of Chemistry and Chemical Engineering, University of Surrey; Guildford, Surrey GU2 7XH, United Kingdom.
d Australian Synchrotron, Australia's Nuclear Science and Technology Organization, Clayton VIC 3168, Australia.
e Dyson School of Design Engineering, Imperial College London, London SW7 2BX, United Kingdom

*Corresponding authors. Email: zaiping.guo@adelaide.edu.au; q.cai@surrey.ac.uk; sailin.liu@adelaide.edu.au

Content

Experimental Section

Preparation of electrodes:

(1) **Zn anode:** All-metallic zinc foil (purity > 99.99%, thickness=100 μm) used in this work was sanded with a softback sanding sponge (3M, 1200 to 1500 Grit) to remove surface oxide layers, followed cleaning with ethanol and drying out in air. Then, the Zn foil was cut into round discs with a diameter of 9.5 mm and an area of 0.709 cm^2 with a hole punch. The Zn foil metal electrode (thickness = 10 μm) is used for the for the test of the cycling stability at a high depth of discharge (DOD).

(2) **Cu electrode:** Cu foil (thickness = 9 μm) was cleaned with ethanol and dried out in air. Then, the Cu foil was cut into round discs with a diameter of 12 mm with a precision disc cutter (MSK-T-10).

(3) **$KV_{12}O_{30-y}\cdot nH_2O$ (KVOH) cathode:** KVOH was synthesized according to previous reports. [1] Typically, 0.364 g of V_2O_5 (Sigma-Aldrich, ≥ 98%) was dissolved into 50 mL of water with 2 mL of H_2O_2 (30%). 0.087 g of K_2SO_4 (Sigma-Aldrich, ≥ 99%) was dissolved into 30 mL of water. Then, the two solutions were mixed under magnetic stirring for 30 min. The mixture was transferred into a 100 mL Teflon-lined stainless-steel autoclave and kept at 120˚C for 6 h. The obtained precipitates were washed with water five times and collected by centrifuge. The washed samples were freeze-dried for 3 days. KVOH was obtained in the form of a green powder. The KVOH cathode electrodes were fabricated by mixing the active material, Super P, and polyvinylidene difluoride (PVDF) binder in a weight ratio of 7:2:1, as well as N-methyl-2-pyrrolidone (NMP). The mixture was carefully ground in a mortar for 1 h to obtain a totally uniform slurry and then casted with a blade on titanium foil (thickness = 10 μm). The prepared electrodes were dried in a vacuum oven at 100°C overnight to remove residual solvent. The as-prepared electrodes were cut into round slices with 9 mm in diameter and a mass loading of ~2 mg cm^{-2}.

(4) **Polyaniline (PANI) cathode:** PANI was synthesized according to previous reports. [2] Typically, 0.365 mL of aniline monomer (Sigma-Aldrich, ≥ 99.5%) was added into 15 mL of 1 M HCl solution under stirring. The mixture was cooled to ~ 0 °C in an ice bath. After stirring for 1 h, 5 mL of 1 M HCl containing 0.228 g of $(NH_4)_2S_2O_8$ (Sigma-Aldrich, ≥ 98%) was added dropwise into the above solution in an ice bath. The colorless solution gradually became dark green. After reacting for 1 h, the sample was washed with water and ethanol, and then dried at 60°C overnight in a vacuum oven. PANI in the form of a dark green powder was thus obtained. The PANI cathode electrode was prepared in same way as the KVOH cathode except for being dried at 60°C for 24 h.

Preparation of electrolytes:

Electrolytes were prepared with the same concentration of 1 m (mol kg^{-1}) by mixing a certain amount of zinc trifluoromethanesulfonate ($Zn(OTf)_2$, Sigma-Aldrich, 98%), diethylene glycol dimethyl ether (G2, Sigma-Aldrich, 99.5%), and water, and were

named according to its volume ratio of G2. For example, the 60%G2 electrolyte contains 60 vol.% G2, 40 vol.% H_2O, and 1 m $Zn(OTf)_2$.

Preparation of pouch cell:

A Zn//KVOH pouch cell consisted of a high-mass-loading KVOH cathode (~ 10 mg cm^{-2}; 3 × 3.5 cm^2), a Zn anode (3.5 × 4.5 cm^2), and a glass fiber separator (4 × 5 cm^2). To prepare the KVOH cathode, 60 wt% active materials were mixed with 20 wt% Super P and 20 wt% polytetrafluoroethylene (PTFE, 60 wt% in H_2O, Sigma-Aldrich), using ethanol as the dispersing agent. The slurry was pressed to form free-standing electrodes and pressed onto titanium mesh (100 mesh) with a rolling machine. The electrode was dried at 60°C overnight.

Characterizations:

Fourier transform infrared (FTIR) spectra were collected on an FTIR spectrometer (Nicolet 6700 ThermoFisher). The FTIR spectra at varying temperatures and *in-situ* FTIR spectra were collected on a Bruker Vertex 80v spectrometer coupled with a Hyperion 3000 FTIR microscope from the Infrared Microspectroscopy (IRM) beamline (Australian Synchrotron). The temperature was controlled by a THMS600 Heating and Freezing stage system. A commercial *in-situ* EL-CELL (ECC-Opto-Std) optical test cell was used to collect *in-situ* FTIR data. The Zn foil metal electrode (thickness = 100 μm) and Ti mesh were cut into strips (2 mm × 10 mm). The electrodes were assembled into the EL-CELL using a sandwich setup according to a previous report. [3] The plating/stripping of zinc on Ti mesh was achieved with a CHI 760 electrochemical workstation. Raman spectra were collected on a Raman spectrometer (HORIBA LabRAM HR Evolution, 532 nm laser). For quantitative analysis, the FTIR spectra were deconvoluted using the Gaussian function with Origin. ^1H and ^{19}F nuclear magnetic resonance (NMR) spectra were collected with an AVANCE III HD 400M NMR. The phase identification was performed by powder X-ray diffractometer (XRD, Rigaku MiniFlex 600, Cu Kα radiation). The morphology of the cycled electrodes and cathode materials was assessed using an FEI Quanta 450 field-emission-gun (FEG) environmental scanning electron microscope (ESEM) equipped with an energy dispersive spectroscopy (EDS) analysis system. Topographic images of surfaces were recorded using a laser confocal microscope (Olympus LEXT OLS5000). Surface compositions of samples were analyzed by X-ray photoelectron spectroscopy (XPS) on a VG Multilab 2000 (VG) photoelectron spectrometer. Electrode samples were prepared using filter paper as separator in coin cells to prevent a silicon signal from glass fiber separator. The electrode was washed with ethanol solvent to remove residual electrolyte before the XPS characterization. Optical *in-situ* observation of zinc dendrite formation on zinc substrates in different electrolytes was conducted in an EL-CELL using the side-by-side setup. Photographs of the monitored area were collected on a Nikon Eclipse E600 POL upright microscope equipped with a charge-coupled device (CCD) camera. The contact angle was determined with an Attension Theta Flow Optical Tensiometer from Biolin Scientific. The pH value of electrolyte was determined with a Thermo Scientific

Orion Versa Star Pro Meter. A differential scanning calorimeter (DSC, Mettler Toledo Differential Scanning Calorimeter 3+) was used to determine the T_t of samples by subjecting them to a temperature range from −80℃ to 10℃ at a heating rate of 5℃ min^{-1}.

Electrochemical Measurements:

The batteries are tested at room temperature (RT) unless otherwise specified. The high- and low-temperature performances of batteries were tested in a temperature-controlled chamber (GWS, MT3065). CR2025 coin cells were assembled in open air with the as-prepared electrolytes (100 μL), glass fiber separators (Filtech Pty Ltd), Zn anodes, and cathodes. All the cells for comparison were basically prepared and tested at the same time to reduce interference. Plating/stripping behavior of the Zn^{2+} was determined using Cu foil as the counter electrode. Charging/discharging tests were carried out on a NEWARE battery tester and a LAND battery tester. The cut-off potentials for Zn//KVOH batteries were set to 0.2 V and 1.6 V, and those for Zn//PANI batteries were 0.5 V and 1.6 V. The applied current density and specific capacity were calculated based on the mass of the cathode. Cyclic voltammetry (CV), linear sweep voltammetry (LSV), and electrochemical impedance spectroscopy (EIS) were performed on Biologic VMP3 Electrochemical Workstations. LSV was conducted in a three-electrode configuration, in which platinum (Pt) foil was the working electrode, Pt electrode was the counter electrode, and Ag/AgCl was the reference electrode at a scan rate of 1.0 mV s^{-1}. The corrosion potential and corrosion current density were obtained by a linear fitting of Tafel plots. The ionic conductivity (σ, mS cm^{-1}) of the electrolytes was measured using electrochemical impedance spectroscopy (EIS, frequency from 200 kHz to 10 mHz) at varying temperatures. The cells were assembled with two stainless steel spacers, a piece of glass fiber separator, and the electrolyte. The conductivity was calculated according to the following equation (1):

$$\sigma = \frac{L}{R \cdot A} \tag{1}$$

σ =L/(R•A), where L (cm) is thickness; A (cm^2) is electrode contact area; and R (Ω) is bulk resistance determined by the intercept with the x-axis in Nyquist plots, respectively.

The activation energy during Zn^{2+} deposition was calculated according to the following Arrhenius equation (2):

$$k = \frac{T}{R_{res}} = Aexp(-\frac{E_a}{RT}) \tag{2}$$

where k is the rate constant; T (K) is absolute temperature; R_{res} (Ω) is ion transfer resistance; A is the preexponential constant; E_a (kJ mol^{-1}) is the activation energy; and R (8.314 $J \cdot mol^{-1} \cdot K^{-1}$) is the standard gas constant. The E_a is obtained by fitting the separated semicircles (R_{sei}, R_{ct}) in Zn//Zn symmetric cells with Zview. R_{sei} represents the resistance of Zn^{2+} across the SEI at medium frequencies. R_{ct} represents the resistance of Zn^{2+} desolvation energy at low frequencies. [4] The Zn//Zn symmetric

cells were assembled and put in the temperature chamber for 20 min at set temperatures before tests.

Galvanostatic intermittent titration technique (GITT) tests were conducted under a small pulse current of 100 mA g^{-1}, with 0.5 h pulse time, and a relaxation period of 2 h for each pulse. The diffusion coefficient (D) of KVOH electrode is calculated from the GITT potential profiles using Fick's second law with the following equation (3):

$$D = \frac{4}{\pi\tau}\left(\frac{n_m V_m}{S}\right)^2\left(\frac{\Delta E_S}{\Delta E_\tau}\right)^2 \quad (3)$$

Where τ is the duration of the current pulse; n_m is the moles of the loaded KVOH electrode material; S is the geometric area of the electrode; V_m is the molar volume of the KVOH; ΔE_S is the quasi-thermodynamic equilibrium potential difference before and after the current pulse; and ΔE_τ is the potential difference during the current pulse.

The resistivity of the Zn electrodes was measured following the formula (5):

$$\rho = \frac{R*S}{L} = \frac{\mathrm{V*S}}{\mathrm{I*L}} \quad (5)$$

where R is the resistance, I is the applied current, V is the corresponding voltage, S is the contact area, and L is the thickness of the electrode.[5]

***Computational details**:*

All molecular dynamics (MD) simulations were performed using the GAFF2 force field. [6] The ACPYPE was employed to obtain the GAFF2 force field topology.[7] The simulation box size of 5 × 5 × 5 nm^3 were used in all simulation models. The simulation systems consist of Zn^{2+}, OTf^-, H_2O, with/without G2 molecules. The ratio of each component is shown in **Table S4**. The cut-off distance of 1.2 nm was used for Lennard-Jones potential. The Coulombic potential was measured using Particle Mesh Ewald (PME) with a cut-off distance of 1.2 nm and Fourier grid spacing of 0.12. All bonds were constrained with LINCS algorithm. Periodic boundary conditions were applied in all directions. The MD simulations were started by running initial energy minimization, followed by 1500 ps of NVT simulation and 1500 ns of NPT simulation with an integration time step of 0.001 ps. All the simulations systems were finally maintained at 298 K using the Nose-Hoover thermostat for 25 ns to collect simulation data. A time constant of 1 ps was applied for the temperature coupling. Several Zn-ion structures observed from the MD simulations were then taken for further investigation using density functional theory (DFT). The DFT calculations were implemented using the Vienna ab-initio simulation package (VASP) [8, 9] with the core and valence electronic interactions being modelled using the projector augmented wave (PAW) method. [10, 11] The Perdew-Burke-Ernzerhof (PBE) exchange-correlation functional was employed. [12] The wavefunction were expanded with a kinetic energy cut-off of 500 eV and a Gamma k-point were used. The dispersion correction was also considered in this study by using DFT-D3 method. [13] Binding energy (BE) between Zn^{2+} and various solvents were calculated using the following equation (4):

$$BE = E_{Zn^{2+}-Solv} - E_{Zn^{2+}} - E_{Solv} \quad (4)$$

where $E_{Zn^{2+}-Solv}$, $E_{Zn^{2+}}$ and E_{Solv} are the total electronic energies of Zn^{2+} ion binds with a solvent molecule, Zn^{2+} ion, and solvent molecule, respectively.

Table S1 Comparison of physical parameters of organic solvents.

The data are from CRC handbook of chemistry and physics. [14]

	Tm (°C)	**Tb (°C)**	**Tf (°C)**	**η (cP) (25°C)**	**DN (kcal mol^{-1})**	**ε**	**Solubility in water (per 100 mL)**
G1	−58	84	−2	0.46	20.0	7.2	miscible
G2 **(this work)**	−64	162	67	1.14	19	7.4	miscible
G3	−44	249	118	3.4	17.2	7.5	miscible
G4	−30	275	141	5.3	16.6	7.5	miscible
DEE	−116.2	34.5	−45	0.22	19.2	4.3	6.05 g
DOX	12	101	12	1.19	14.3	2.3	miscible
EC	36	248	160	1.9 (40°C)	16.4	89.7	77.8 g
PC	−48	242	132	2.53	15.1	64	24 g
GBL	−44	206	99.2	1.7	18	41	miscible
DMC	0.5	91	17	0.43	17.2	3.1	13.9 g
DEC	−74	126	31	0.75	16	2.8	1.88 g
EMC	−14	107	23	0.64	6.5	2.99	4.68 g
THF	−108.5	66	−14	0.52	20	7.58	miscible
DMSO	18.4	189	89	1.987	29.8	47.24	miscible
TMP	−46	197	107	0.45	23	21.6	miscible

T_m: melting point
T_b: boiling point
T_f: flash point

η: viscosity
DN: donor number
ε: dielectric constant

G1: 1,2-dimethoxyethane
G2: diethylene glycol dimethyl ether
G3: triethylene glycol dimethyl ether
G4: tetraethylene glycol dimethyl ether
DEE: diethyl ether
DOX: 1,4-Dioxane
EC: ethylene carbonate
PC: propylene carbonate

GBL: γ-butyrolactone
DMC: dimethyl carbonate
DEC: diethyl carbonate
EMC: ethyl methyl carbonate
THF: tetrahydrofuran
DMSO: dimethyl sulfoxide
TMP: trimethyl phosphate

Table S2 Binding energy of solvent and Zn^{2+} cation from DFT calculation.

	Binding Energy (eV)
G1	−0.23
G2	−0.45
G3	−0.44
G4	−0.11
DEE	−0.37
DOX	−0.50
EC	−0.77
PC	−0.79
GBL	−0.96
DMC	−0.40
DEC	−0.13
EMC	−0.36
THF	−0.36
DMSO	−1.27
TMP	−0.93

Table S3 Prices of solvents.

Price data are from Sigma Aldrich (https://www.sigmaaldrich.com/US/en) and normalized according to density data from Wikipedia (https://en.wikipedia.org/wiki).

Solvent	Sigma Aldrich SKU	Sigma Aldrich SKU Online price (US$)	Normalized Price (US$ kg^{-1})
G1	E27408	190/L	219
G2 (this work)	M14102	163/L	174
G3	T59803	49.6/250 g	201
G4	172405	168/kg	168
DEE	673811	192/L	269
DOX	360481	140/L	136
EC	E26258	33.4/500g	67
PC	P52652	79.8/500g	160
GBL	B103608	64/500g	128
DMC	D152927	55.6/500g	111
DEC	517135	186/L	191
EMC	809934	982/500g	1964
THF	360589	139/L	157
DMSO	276855	336/L	305
TMP	241024	36.4/50g	728

Table S4 Components of electrolytes.

Electrolyte	Component			
	v (H_2O)/ (mL)	v (G2)/ (mL)	c ($Zn(OTf)_2$)/ ($mol \cdot kg^{-1}$)	n (H_2O) : n (G2)
0%G2	1000	0	1	-
20%G2	800	200	1	32 : 1
40%G2	600	400	1	12 : 1
60%G2	400	600	1	5 : 1
80%G2	200	800	1	2 : 1
100%G2	0	1000	1	-

Table S5 Coordination number of Zn^{2+} with H_2O/G2/OTf^- in different electrolytes.

Component \ Electrolyte	0%G2	60%G2	80%G2
H_2O	5.6	5	3.7
G2	0	0.074	1.06
OTf^-	0.4	1	1.2

Table S6 Number of components in the electrolytes in MD simulation.

Components \ Electrolyte	Number of each component		
	0%G2	**60%G2**	**80%G2**
Zn^{2+}	60	54	54
OTf^-	120	108	108
G2	-	217	302
H_2O	3340	1200	599

Table S7 Comparison of cumulative plating capacity (CPC) of this work with recently reported Zn//Zn symmetric cells.

The electrodes are all Zn foil.

No.	Electrolyte	Testing conditions (mA cm^{-2}/mAh cm^{-2})	CPC (Ah cm^{-2})	Ref.
/	1 m $Zn(OTf)_2$ + 60 vol.% G2 + 40 vol.% H_2O	1, 1	3.75	This work
		5, 5	1.2	
1	2 M $Zn(OTf)_2$ + 25 wt.% G4 + 75 wt.% H_2O	0.5, 0.5	1.125	[15]
2	2 M $ZnSO_4$ + 3 vol.% DGME + 97 vol.% H_2O	0.5, 0.25	0.75	[16]
3	0.2 m $Zn(OTf)_2$ + 1.6 m NaOTf + 45.8 mol% DOX + H_2O	0.5, 2	1.25	[17]
4	1 M $Zn(OTf)_2$ + 50 vol.% DOL + 50 vol.% H_2O	0.5, 0.5	0.375	[18]
		1, 1	0.49	
5	1 M $Zn(OTf)_2$ + 50 vol.% PC + 50 vol.% H_2O	1, 1	0.8	[19]
6	2 m $Zn(OTf)_2$ + 40 wt.% MA + 60 wt.% H_2O	1, 1	2.3	[20]
7	1 M $Zn(OTf)_2$ +50 vol.% AC + 50 vol.% H_2O	1, 1	0.45	[21]
8	0.5 M $Zn(OTf)_2$ + 50 vol.% TEP + 50 vol.% H_2O	1, 1	0.75	[5]
9	2 M $ZnSO_4$ + 40 vol.% EG + 60 vol.% H_2O	2, 1	0.14	[22]
10	1.6 m $ZnCl_2$ + 18.8 vol.% DMSO + 81.2 vol.% H_2O	0.5, 0.5	0.25	[23]
11	0.2 m $Zn(OTf)_2$ + 30 vol.% 2-propanol + 70 vol.% H_2O	1, 1	1.5	[24]
12	2 M $Zn(OTf)_2$+30 vol.% DMF+ 70 vol.% H_2O	0.5, 0.5	0.5	[25]
13	1 m $Zn(OTf)_2$ + 30 vol.% H_2O + 70 vol.% THFA	1, 1	1.375	[26]
14	2 M $Zn(OTf)_2$ + 20 vol.% TMU + 80 vol.% H_2O	1, 1	1.4	[27]
15	2 m $ZnSO_4$ + 20 vol.% DMSO + 80 vol.% H_2O	1, 1	1.05	[28]
16	0.5 M $ZnSO_4$ + 12.5 vol.% Butanone + 87.5 vol.% H_2O	1, 1	1.125	[29]

G4: tetraethylene glycol dimethyl ether
DGME: diethylene glycol monomethyl ether
DOX: 1,4-dioxane
DOL: 1,3-dioxolane
PC: propylene carbonate
MA: methyl acetate
AC: acetone
TEP: triethyl phosphate
EG: ethylene glycol

DMF: N,N-Dimethylformamide
THFA: tetrahydrofurfuryl alcohol
TMU: tetra-methyl-urea
DMSO: dimethyl sulfoxide

M: mol L^{-1}
m: mol kg^{-1}

Table S8 Relative texture coefficient ($RTC_{(hkl)}$) of different Zn electrode.
The calculated relative texture coefficient ($RTC_{(hkl)}$) of crystal planes of different Zn electrode.

	(002)	(100)	(101)	(102)	(103)	(110)
Pristine Zn	6.4	11.8	15.7	31.3	23.0	11.8
0%G2_20 cycles	6.2	11.0	15.6	30.2	27.9	10.9
60%G2_20 cycles	29.3	7.7	9.2	20.8	26.4	6.5
60%G2_100 cycles	33.5	7.2	9.5	19.8	23.9	6.2
60%G2_200 cycles	42.5	6.1	7.7	17.6	21.8	4.2

The preferred orientations for Zn deposition were determined by calculating the $RTC_{(hkl)}$ according to the equation: [30, 31]

$$RTC_{(hkl)} = \frac{I_{(hkl)}/I_{0(hkl)}}{\sum (I_{(hkl)}/I_{0(hkl)})} \times 100$$

where $I_{(hkl)}$ is the peak intensity of zinc electrodeposits and $I_{0(hkl)}$ represents the intensities for the standard Zn sample taken from a powder diffraction file (PDF) card (PDF# 99-0110).
The Zn electrodes were cycled in electrolytes at 1 mA cm^{-2}, 1 mAh cm^{-2}.

Table S9 Summary of electrolytes using co-solvent strategy for ZIBs operating within wide temperature range.

No.	Electrolyte	Operating temperature range (℃)	Cathode	Cycling performance					Ref.
				Capacity (mAh g^{-1})	Capacity retention	Cycle number	Current density (A g^{-1})	Temperature (℃)	
/	1 m $Zn(OTf)_2$ + 40 vol.% H_2O + 60 vol.% G2	−45 to +60	KVOH	160	91.2%	8000	5.0	RT	This work
				110.7	90.1%	2400	0.1	−45	
				307	86.5%	1200	5.0	60	
1	0.2 m $Zn(OTf)_2$ + 70 vol.% H_2O + 30 vol.% 2-propanol	−20 to +25	V_2O_5	375	69.5%	2000	1.0	25	24
				175	88.8%	2000	1.0	−20	
2	2 M $ZnSO_4$ + 40 vol.% EG + 60 vol.%H_2O	−20 to +20	PANI-V_2O_5	~160	49.4%	−	1	20	22
				~100	−	275	0.2	−20	
3	2 M $ZnSO_4$+50 vol.% EG+ 50 vol.% H_2O	−40 to +80	PQ-MCT	88	−	900	0.2	60	32
4	3 M $ZnSO_4$ + 20 vol.% PG + 80 vol.% H_2O	−20 to +25	V_2O_5	348	92.5%	5000	0.5	25	33
				~240	79.1%	500	0.5	−20	
5	2 M $ZnSO_4$ + 50 vol.% MeOH + 50 vol.%H_2O	−20 to +60	PANI	186.3	89.3%	2000	5	−10	34
				219.1	85.5%	2000	5	25	
6	1 vol.% Et_2O + 30 vol.% EG + 2 M $ZnSO_4$ + 0.2 M $MnSO_4$ + H_2O	−10 to +25	CNT/MnO_2	~125	~72%	500	3	25	35
				~95	69.1%	500	3	−10	
7	1 M $Zn(OTf)_2$ + 50 vol.% DOL + 50 vol.% H_2O	−30 to RT	$V_2O_5 \cdot 1.6H_2O$	131	−	300	0.1	−30	18
8	1 M $Zn(OTf)_2$ + 72 vol. % AN+ 28 vol. % H_2O	−40 to +25	V_2O_5	114	−	−	0.05	−40	36
9	3 m $Zn(OTf)_2$ + 20 vol.% PC+80 vol.% H_2O	−40 to +30	$NaV_3O_8 \cdot 1.5H_2O$	183	~100%	300	0.1	−40	37

10	1 m $Zn(OTf)_2$ + 30 vol.% H_2O + 70 vol.% THFA	−40 to +60	VO_2	~80	~100%	200	0.06	−40	[26]
				216.56	93.45%.	1500	0.5	25	
				273	86.71%	500	3.0	60	
11	2 m $ZnSO_4$ + 20 vol.% DMSO + 80 vol.% H_2O	−20 to RT	MnO_2	107	65.4%	300	1 C	−20	[28]

RT: room temperature
EG: ethylene glycol
PG: 1,2-propanediol
MeOH: methanol
Et_2O: ethyl ether
DOL: 1,3-dioxolane
AN: acetonitrile
PC: propylene carbonate
THFA: tetrahydrofurfuryl alcohol
DMSO: dimethyl sulfoxide
M: mol L^{-1}
m: mol kg^{-1}

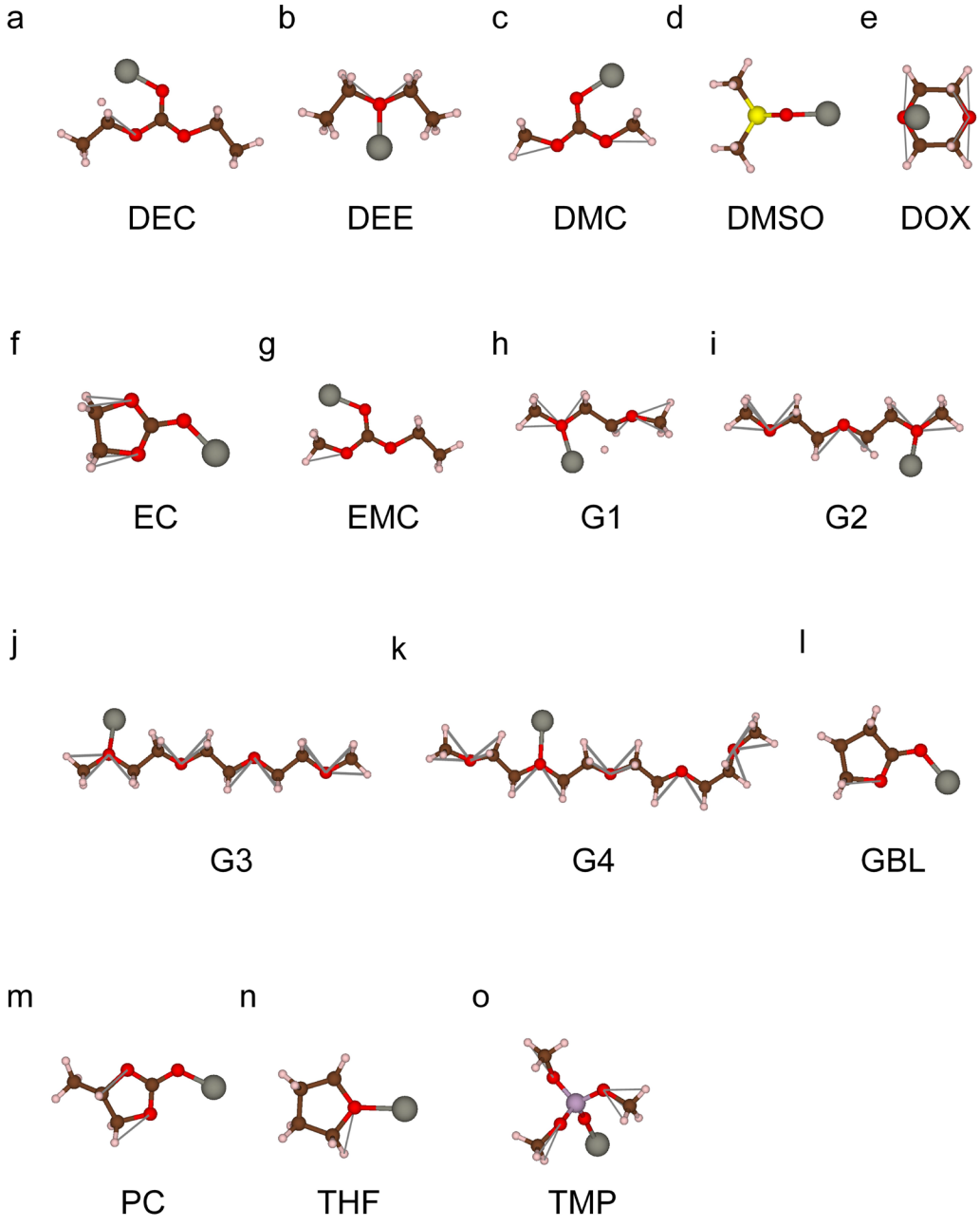

Fig. S1 Optimized geometries of the Zn^{2+}–solvent complexes from the DFT calculations of binding energy between Zn^{2+} and solvent.

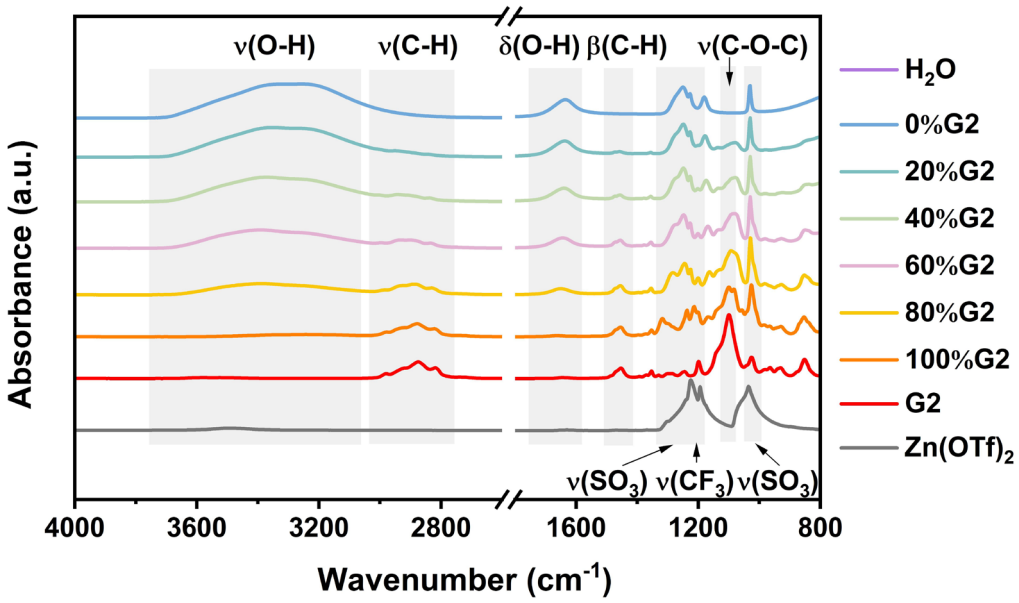

Fig. S2 FTIR spectra.

FTIR spectra and characteristic peaks of $Zn(OTf)_2$, G2, H_2O, and hybrid electrolytes. Solid $Zn(OTf)_2$ salt exhibits three strong peaks within the range of 1000 to 1350 cm^{-1}, corresponding to the symmetric stretching vibration of SO_3 ($\nu_s(SO_3)$, ~1040 cm^{-1}), the asymmetric stretching vibration of CF_3 ($\nu_{as}(CF_3)$, ~1190 cm^{-1}), and the symmetric stretching vibration of CF_3 ($\nu_s(CF_3)$, ~1225 cm^{-1}). Upon dissolution, a new band around 1270 cm^{-1} representing "free" $\nu_{as}(SO_3)$ emerges. [38]

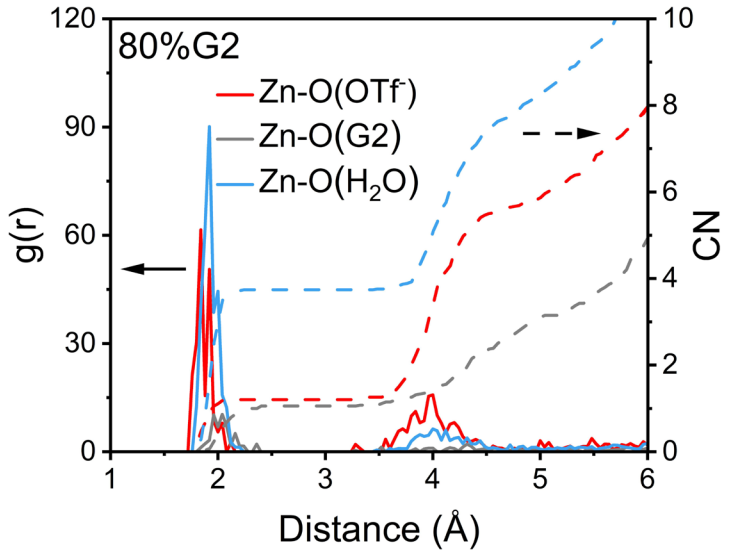

Fig. S3 MD simulation of 80%G2 electrolyte.

The radial distribution functions (RDFs) and coordination numbers (CNs) of Zn^{2+}-O in 80%G2 electrolyte.

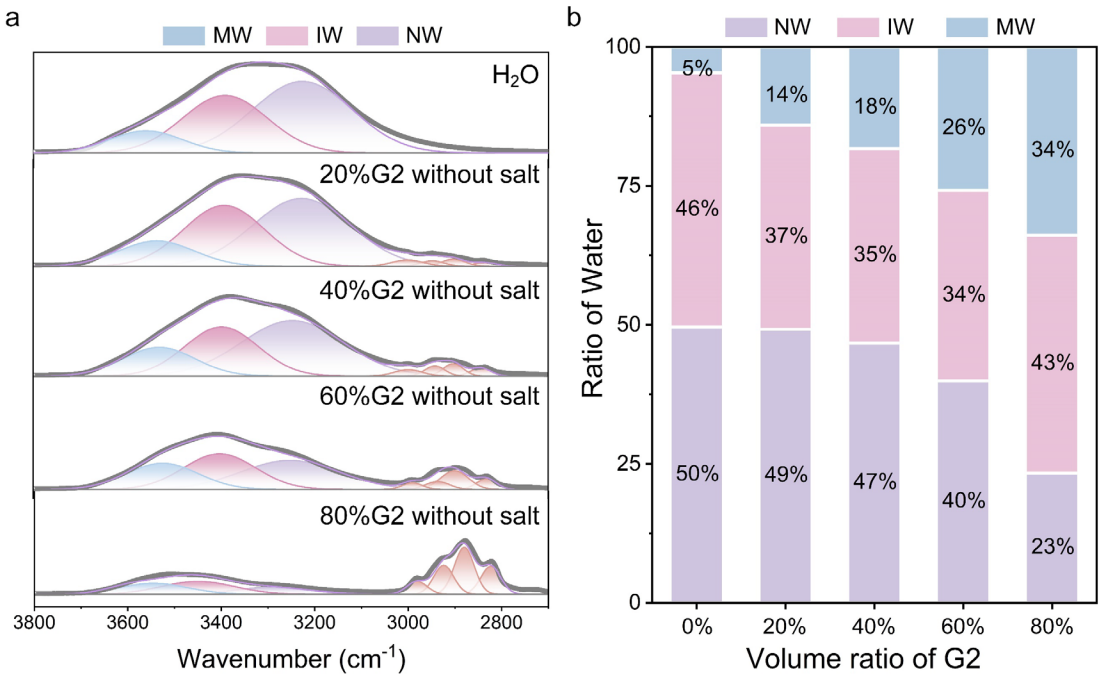

Fig. S4 FTIR spectra of mixtures of G2 and H_2O without salt at room temperature.

(a) The FTIR spectra of H_2O−G2 solutions with varying G2 ratios, without salt in the region from 2700 to 3800 cm^{-1}. Here, 20%G2 without salt indicates that 20% of the volume of the mixture is G2. The peaks correspond to network water (NW), intermediate water (IW), and multimer water (MW) (b) A comparison of the areal ratios of NW, IW, and MW in electrolytes obtained from fitting accumulated peaks between 2700 and 3800 cm^{-1} with different volume ratios of G2.

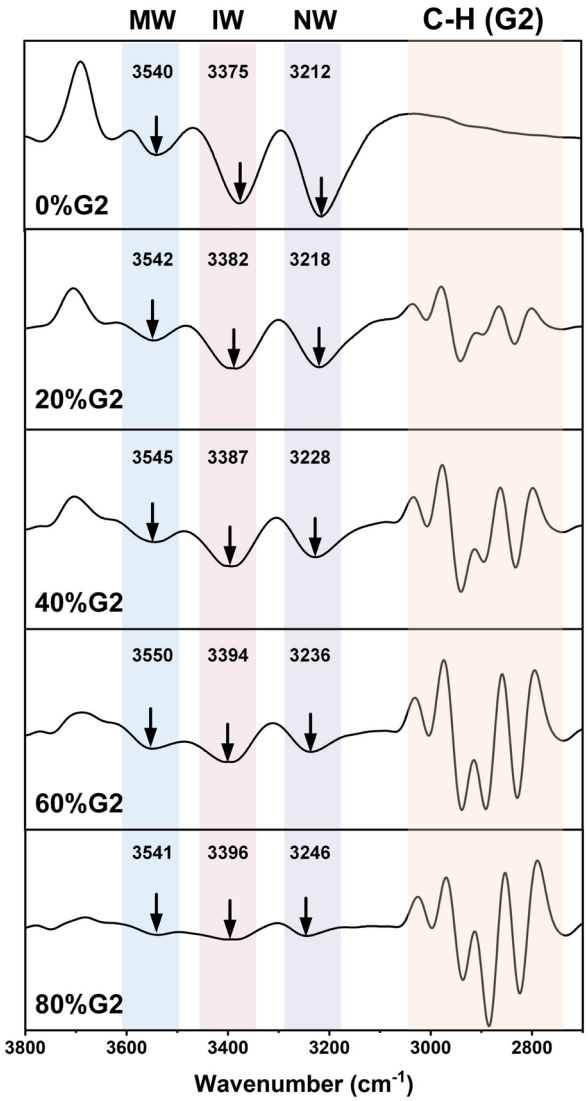

Fig. S5 Second derivatives FTIR spectra.

Second derivatives of FTIR absorption for electrolytes in the region from 3800 to 2700 cm^{-1}. The blue, pink, and purple range within 3000-3800 cm^{-1} represents peaks from MW, IW, and NW, respectively. The orange range within 2700-3000 cm^{-1} represent the C-H (-CH_2- and -CH_3) bonds in G2.

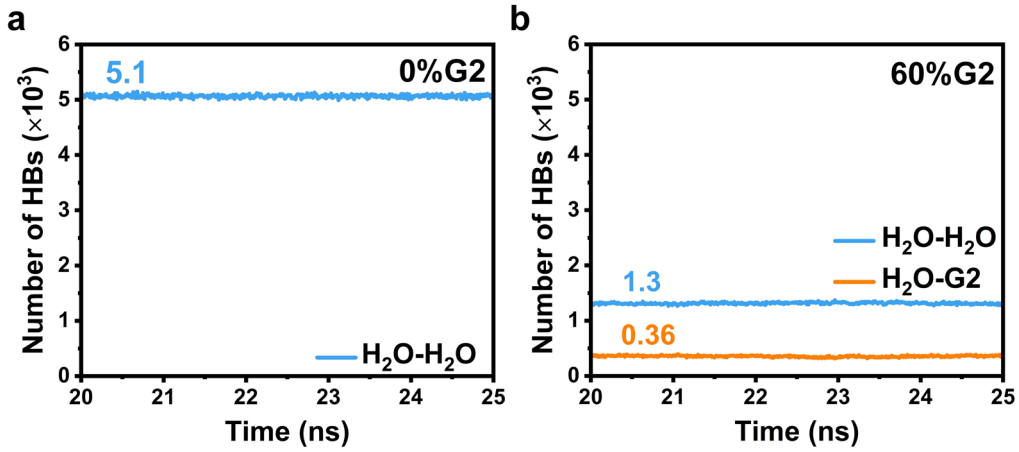

Fig. S6 Molecular dynamics simulations of HBs evolution.

The number of HBs between water molecules (H_2O−H_2O), and water molecules−G2 (H_2O−G2) during the simulation time between 20 and 25 ns in (a) 0%G2 and (b) 60%G2 electrolytes.

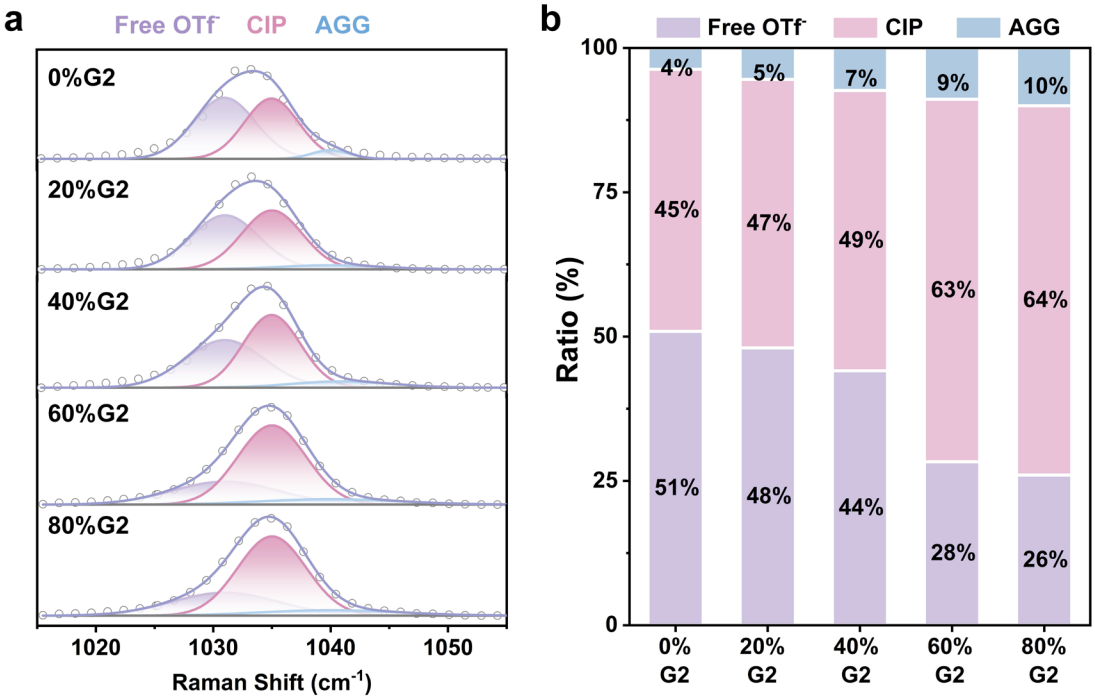

Fig. S7 Raman spectra in the region from 1015 to 1055 cm^{-1}.

(a) Raman spectra of electrolytes in the region from 1015 to 1055 cm^{-1}, which includes ν_s (SO_3) from OTf^-. (b) Comparison of the fitted areal ratios of free OTf^-, contact ion pairs (CIP), and aggregate cation–anion pairs (AGG) by fitting accumulated Raman peak areas of ν_s (SO_3) in 0%G2, 20%G2, 40%G2, 60%G2, and 80%G2 electrolytes.

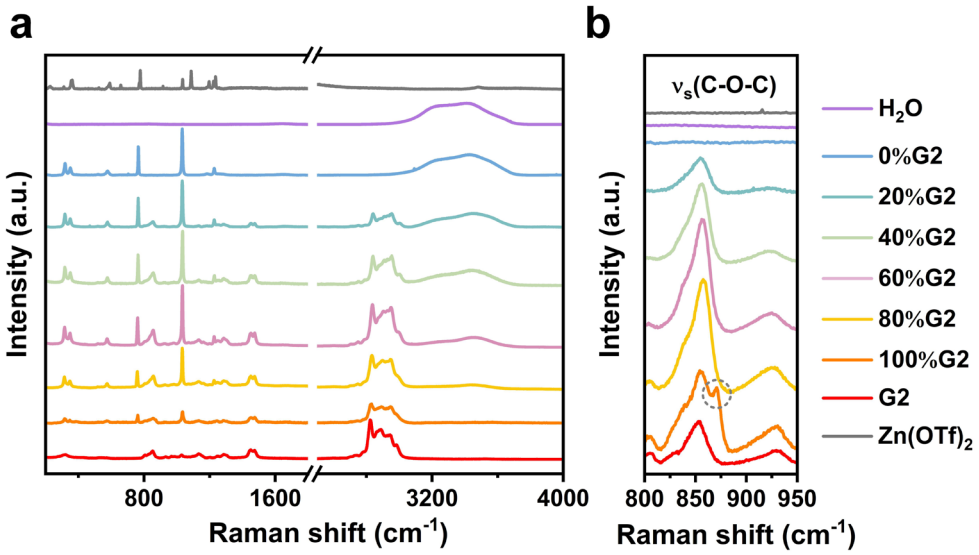

Fig. S8 Raman spectra.

Raman spectra of (a) $Zn(OTf)_2$, G2, H_2O, and hybrid electrolytes and (b) ν_s(C-O-C) in electrolytes.

The appearance of a new peak (shown in the dashed grey circle) in 100% G2 indicates the strong coordination of Zn^{2+} and G2.

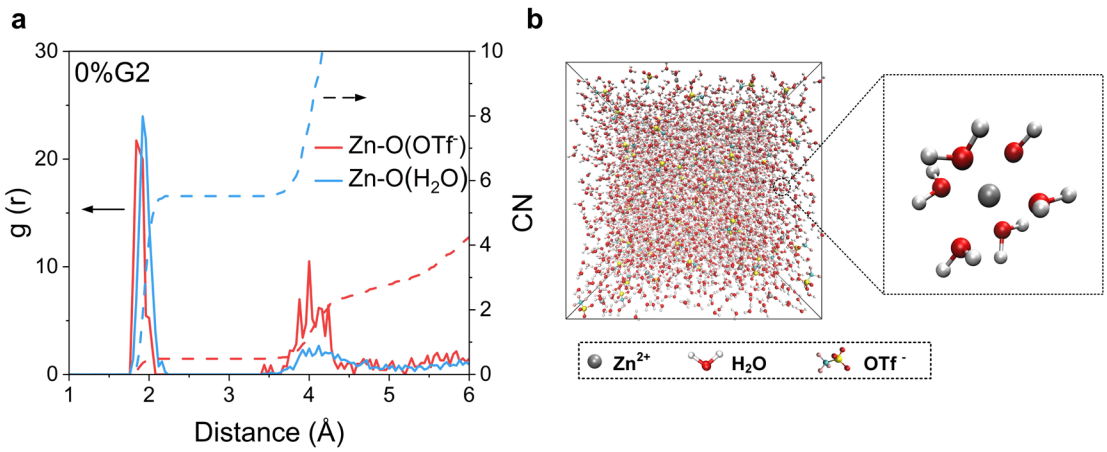

Fig. S9 MD simulation of 0%G2 electrolyte.

(a) RDFs and CNs of Zn^{2+} with O from OTf^- and H_2O in 0%G2 electrolyte. (b) 3D snapshots captured from the MD simulations and schematic illustrations of the Zn^{2+} inner solvation sheath.

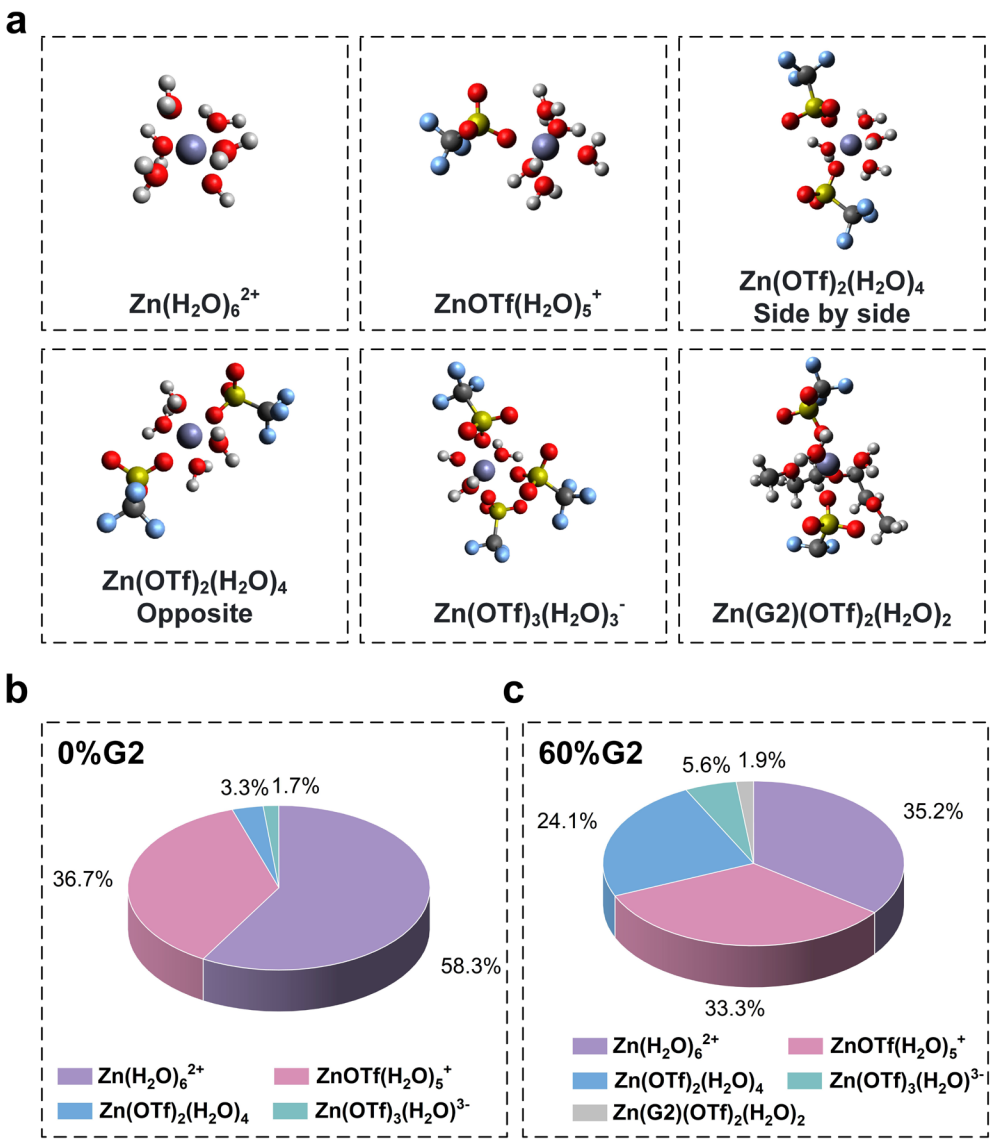

Fig. S10 Solvent-anion coordination from MD simulation.

(a) Solvation structure extracted from MD simulation of the 60%G2 electrolyte. Ratio of Zn^{2+} coordination environments with OTf^{-}, G2 and H_2O in (b) 0%G2 and (c) 60%G2 electrolytes.

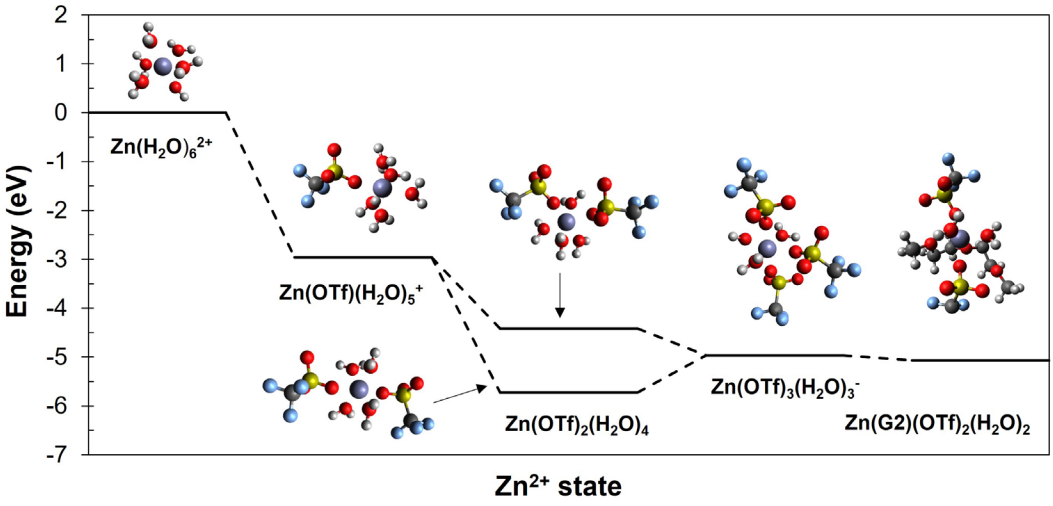

Fig. S11 Gibbs free energy of different complexes.

Gibbs free energy of different complexes in the 60%G2 electrolyte.

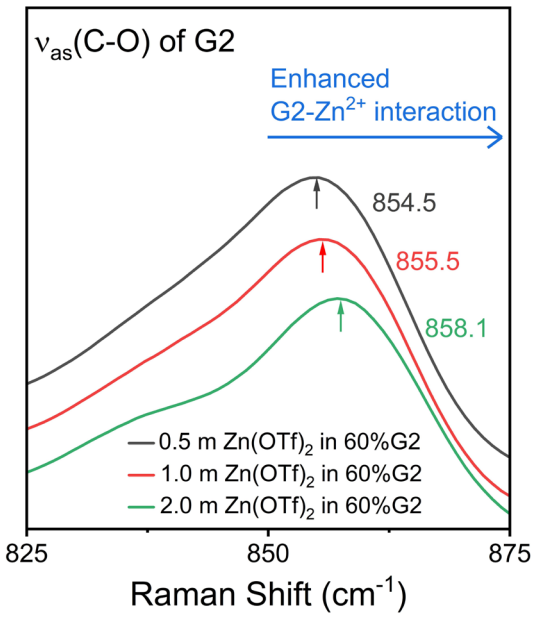

Fig. S12 The Raman spectrum of 60%G2 with 0.5 m, 1 m, and 2 m $Zn(OTf)_2$.

The increased Raman shift for C-O-C peak from 854.5 cm^{-1} (60%G2 with 0.5 m $Zn(OTf)_2$) to 858.1 cm^{-1} (60%G2 with 2 m $Zn(OTf)_2$) indicates the intensified Zn^{2+}–G2 interaction.

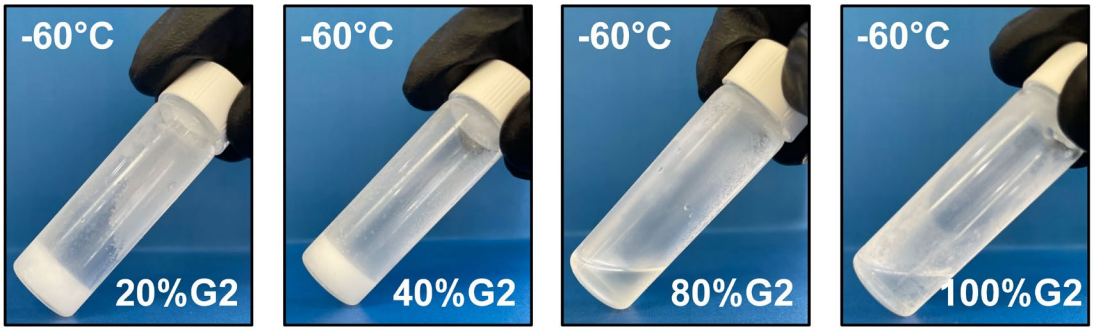

Fig. S13 Optical images of electrolytes stored under −60°C.

Optical images of 20%G2, 40%G2, 80%G2, and 100%G2 electrolytes stored under −60°C.

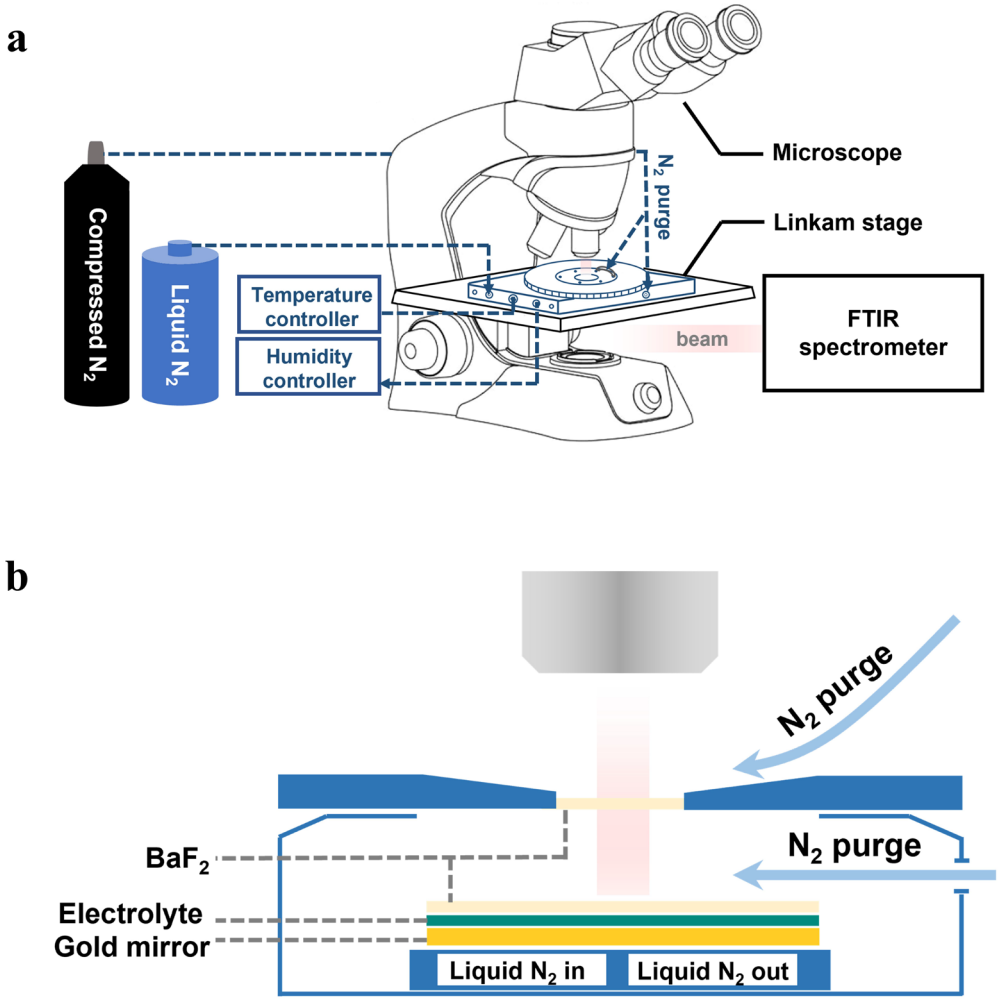

Fig. S14 Illustration of FTIR spectrometer and Linkam temperature control stage.

(a) Setup for the combined use of FTIR spectroscopy and a Linkam stage. (b) Enlarged image of the Linkam stage under varying temperature conditions.

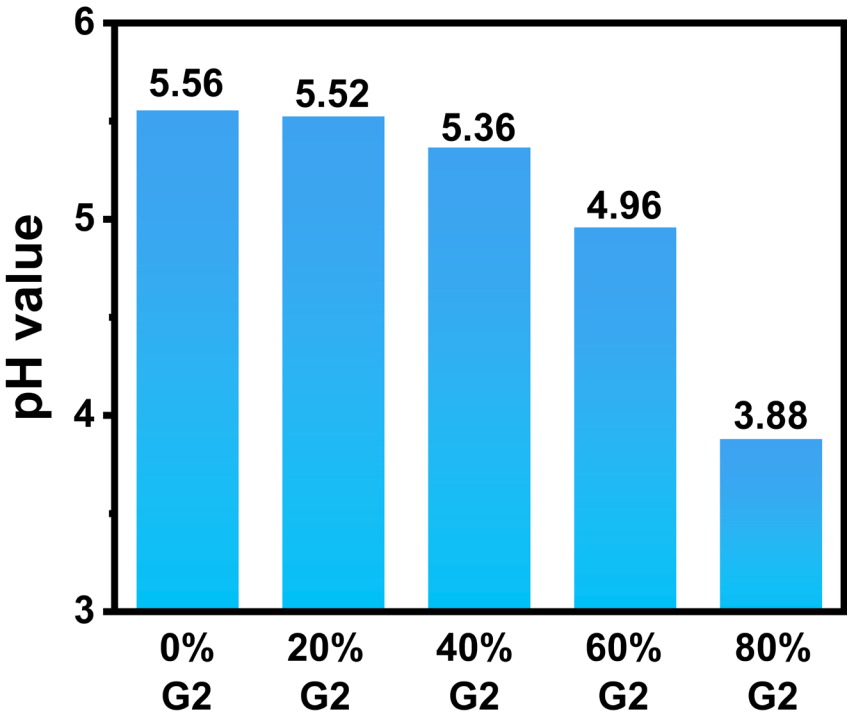

Fig. S15 The pH values of electrolytes.

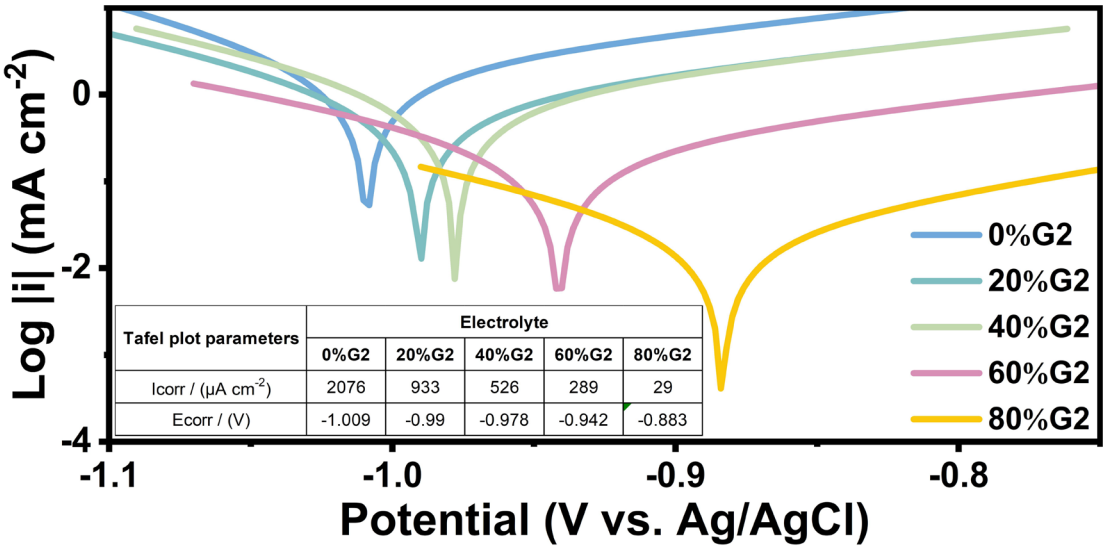

Tafel plot parameters	Electrolyte				
	0%G2	20%G2	40%G2	60%G2	80%G2
Icorr / (μA cm^{-2})	2076	933	526	289	29
Ecorr / (V)	-1.009	-0.99	-0.978	-0.942	-0.883

Fig. S16 Tafel plots of Zn electrode in the electrolytes.

Tafel plots, I_{corr} (corrosion current), and E_{corr} (corrosion potential) in electrolytes, which were collected with Zn foil, Pt, and Ag/AgCl as working electrode, counter electrode, and reference electrode, respectively.

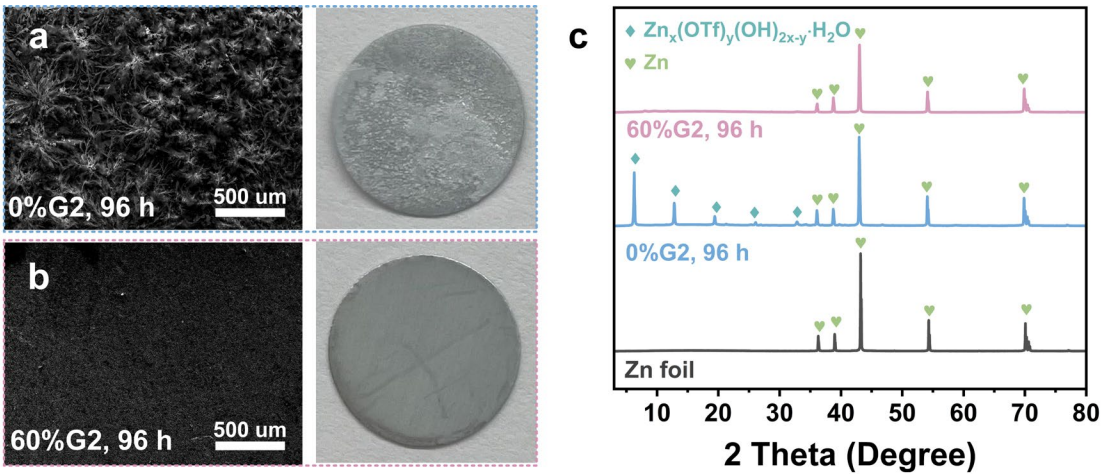

Fig. S17 Chemical corrosion on Zn in 0%G2 and 60%G2 electrolytes.

Scanning electron microscope (SEM) images and photographs of Zn foil immersed in (a) 0%G2 and (b) 60%G2 electrolytes for 96 h, and the corresponding (c) XRD patterns.

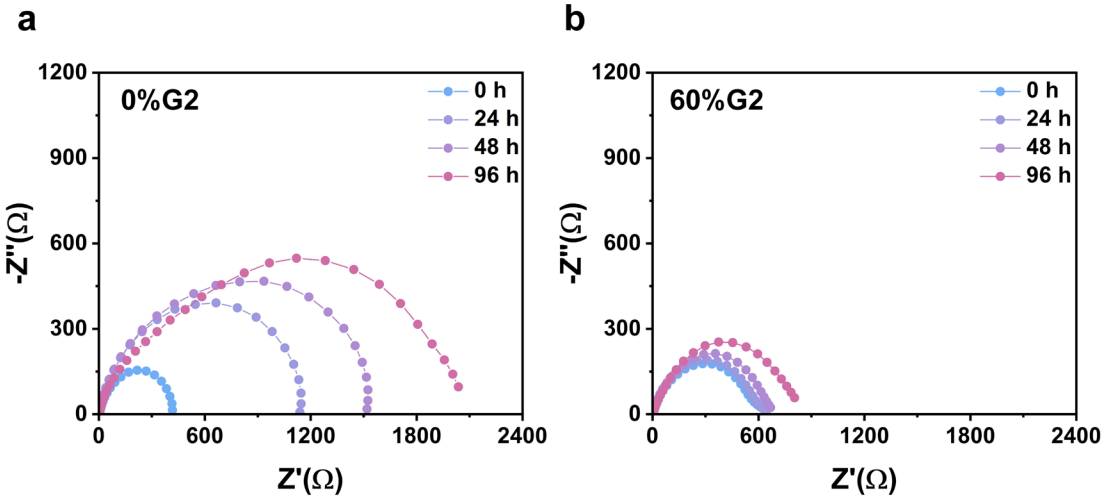

Fig. S18 Electrochemical characterization of chemical corrosion on Zn in electrolytes.

Electrochemical impedance spectra (EIS) of Zn//Zn symmetric cells rested at RT for different times in (a) 0%G2 and (b) 60%G2 electrolytes.

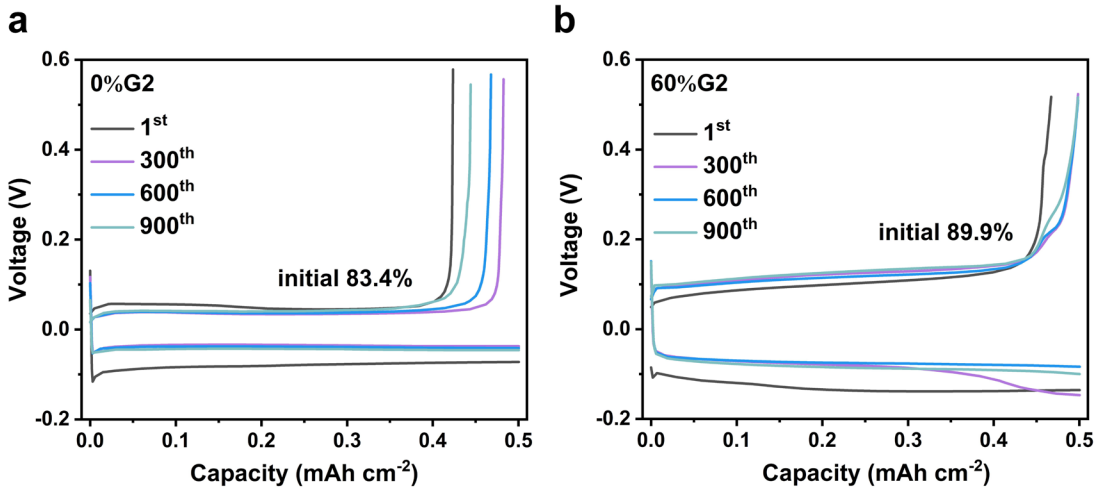

Fig. S19 Zn plating/stripping profiles of Zn//Cu asymmetric cells.

Zn plating/stripping profiles of Zn//Cu asymmetric cells in (a) 0%G2 and (b) 60%G2 electrolytes at current density of 2 mA cm^{-2}, areal capacity of 0.5 mAh cm^{-2} at the 1^{st}, 300^{th}, 600^{th}, and 900^{th} cycles.

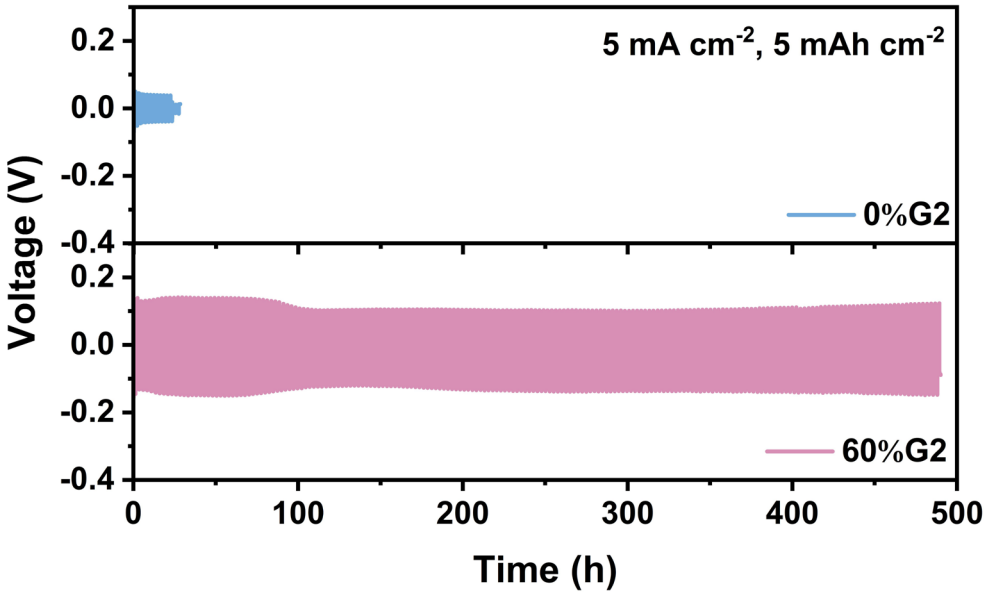

Fig. S20 Cycling performance of Zn//Zn symmetric cells at 5 mA cm^{-2}, 5 mAh cm^{-2}.

Voltage profiles of galvanostatic plating/stripping of Zn//Zn symmetric cells with 0%G2 and 60%G2 electrolytes at current density of 5 mA cm^{-2}, areal capacity of 5 mAh cm^{-2}.

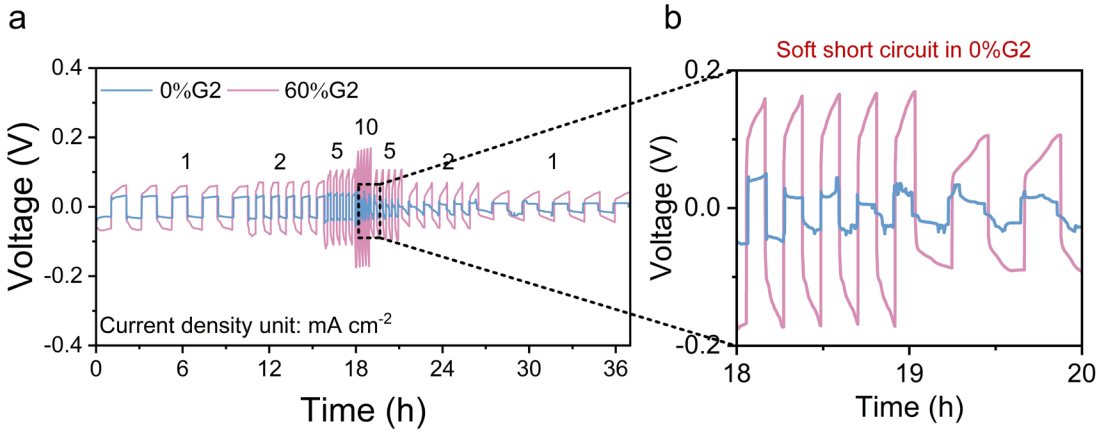

Fig. S21 High-rate tests of Zn//Zn symmetric cells.

Rate tests of Zn//Zn symmetric cells with 0%G2 and 60%G2 electrolytes at different current densities (1-10 mA cm^{-2}) and 1 mAh cm^{-2} capacity at room temperature.

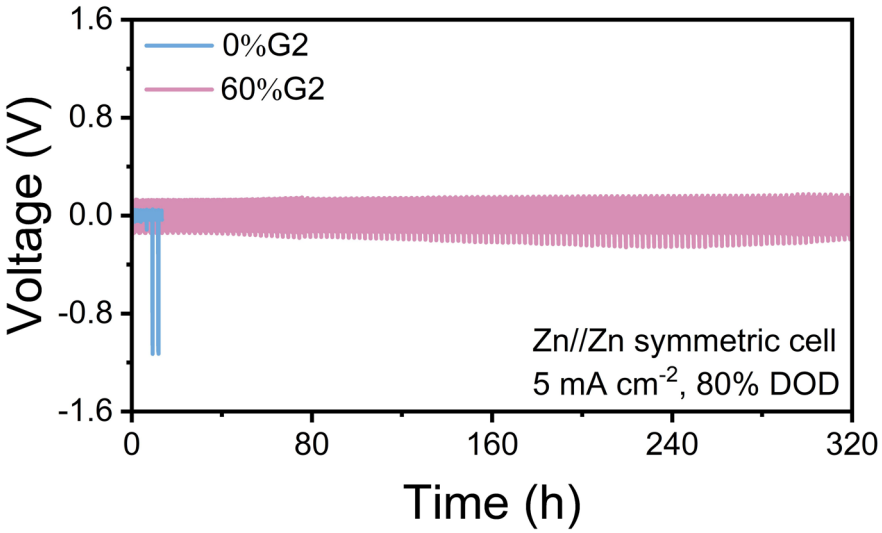

Fig. S22 Cycling performance of Zn//Zn symmetric cells at 80% depth of discharge (DOD).

Long-term cycling performance of Zn//Zn symmetric cells in 0%G2 and 60%G2 at 80% Zn utilization.

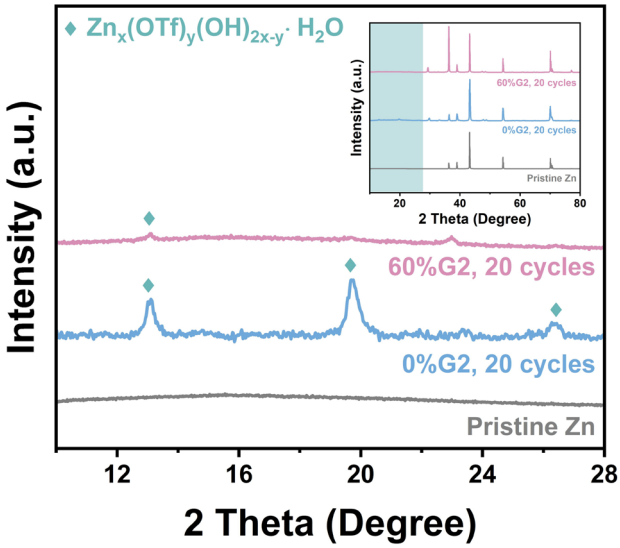

Fig. S23 Characterization of by-product on Zn after cycling.

Enlarged view of XRD patterns (with full patterns in the inset) of pristine Zn, and Zn anodes cycled in 0%G2, 60%G2 electrolytes for 20 cycles at current density of 1 mA cm^{-2}, areal capacity of 1 mAh cm^{-2}.

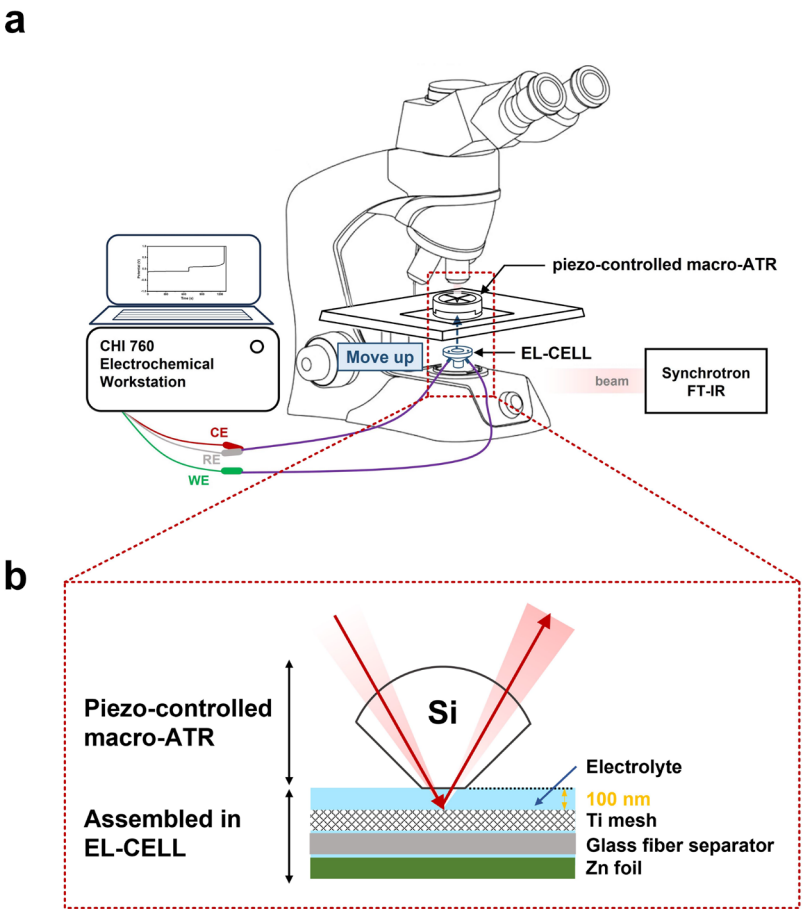

Fig. S24 Schematic illustration of *in-situ* FTIR spectra collection.

(a) The setup of piezo-controlled macro-ATR for *in-situ* monitoring interfacial area of electrode by Synchrotron FTIR. (b) Enlarged image of Si crystal and the "sandwich" setup in EL-CELL.

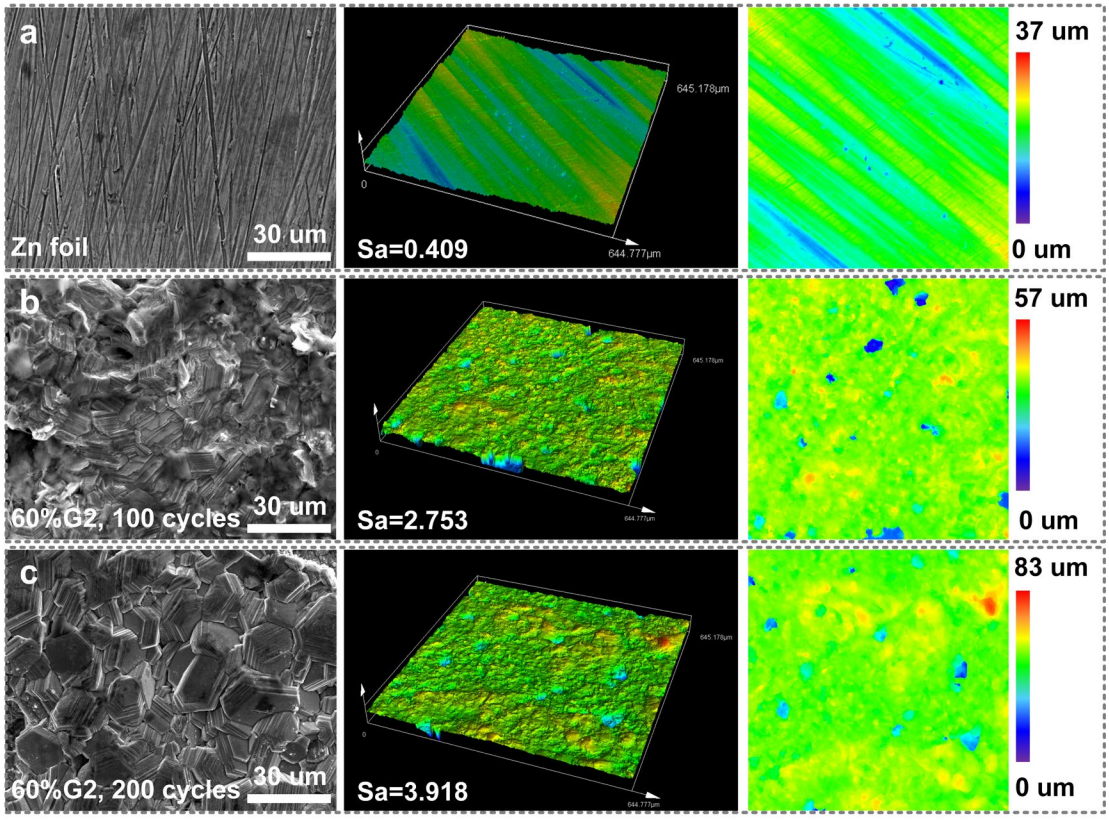

Fig. S25 SEM and 3D reconstruction images of Zn electrode.

SEM images, corresponding 3D reconstruction images, mapping images, and arithmetical mean height (S_a) values of (a) Zn foil, and Zn electrodes cycled in 60%G2 electrolyte for (b) 100 and (c) 200 cycles at current density of 1 mA cm^{-2}, areal capacity of 1 mAh cm^{-2}.

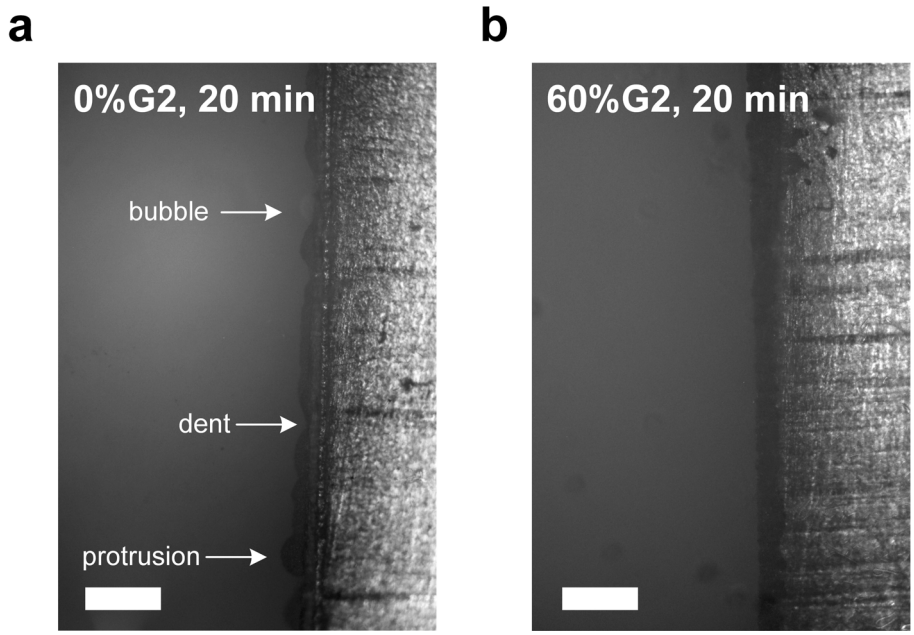

Fig. S26 *In-situ* observation of Zn deposition with optical microscope.

In-situ optical microscope image at lower magnification of Zn deposition on Zn foil in (a) 0%G2 and (b) 60%G2 electrolytes after 20 min (scale bar = 200 μm).

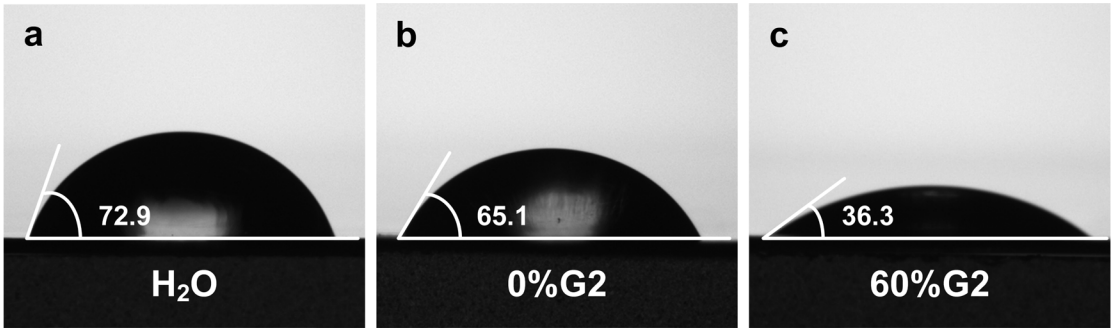

Fig. S27 Contact angles.

Contact angles of (a) H_2O, (b) 0%G2 electrolyte, and (c) 60%G2 electrolyte on pristine Zn.

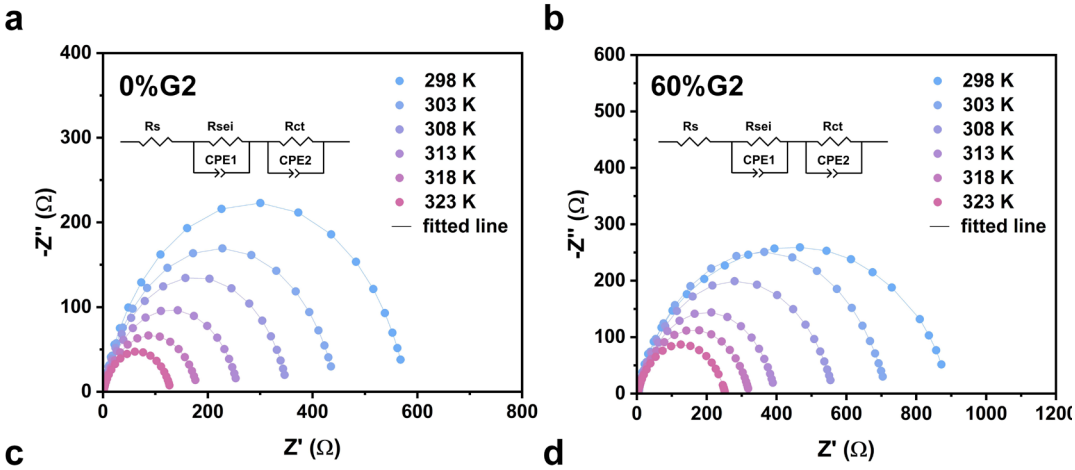

c

T (K)	1000/T (K^{-1})	Rct (Ω)	ln(T/Rct)
298.15	3.3540	579.6	-0.6647
303.15	3.2987	444.5	-0.3827
308.15	3.2452	352.3	-0.1339
313.15	3.1934	258.1	0.1933
318.15	3.1432	180.9	0.5646
323.15	3.0945	130.0	0.9106

d

T (K)	1000/T (K^{-1})	Rct (Ω)	ln(T/Rct)
298.15	3.3540	823.4	-1.0158
303.15	3.2987	713.8	-0.8564
308.15	3.2452	561.4	-0.5998
313.15	3.1934	392.5	-0.2259
318.15	3.1432	320.1	-0.0061
323.15	3.0945	251.3	0.2515

Fig. S28 Activation energy of desolvation of Zn^{2+} in 0%G2 and 60%G2 electrolytes.

Nyquist plots at various temperatures for Zn//Zn cells in (a) 0%G2 and (b) 60%G2 electrolytes. Insets show the equivalent circuit model used for fitting. Corresponding values of R_{ct} at various temperatures for (c) 0%G2 and (d) 60%G2 electrolytes.

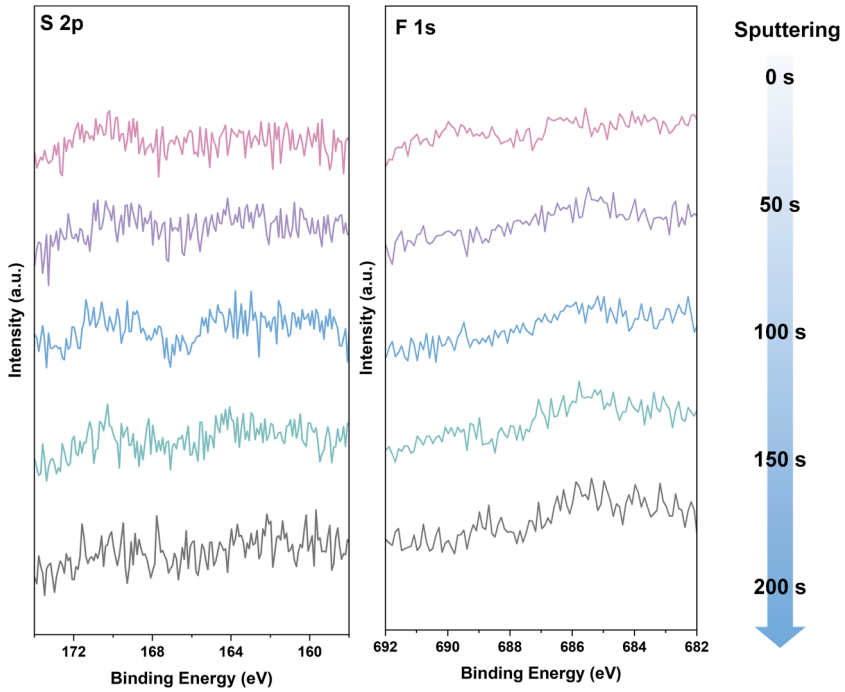

Fig. S29 XPS spectra of S 2p and F for Zn cycled in 0%G2 electrolyte.

Ar^+ sputtering for 0s, 50s, 100s, 150s, and 200s was conducted to generate depth profiles. Zn anode samples were obtained from Zn//Zn symmetric cells with 0%G2 electrolyte after 20 cycles of stripping/plating (1 mA cm^{-2}, 1 mAh cm^{-2}).

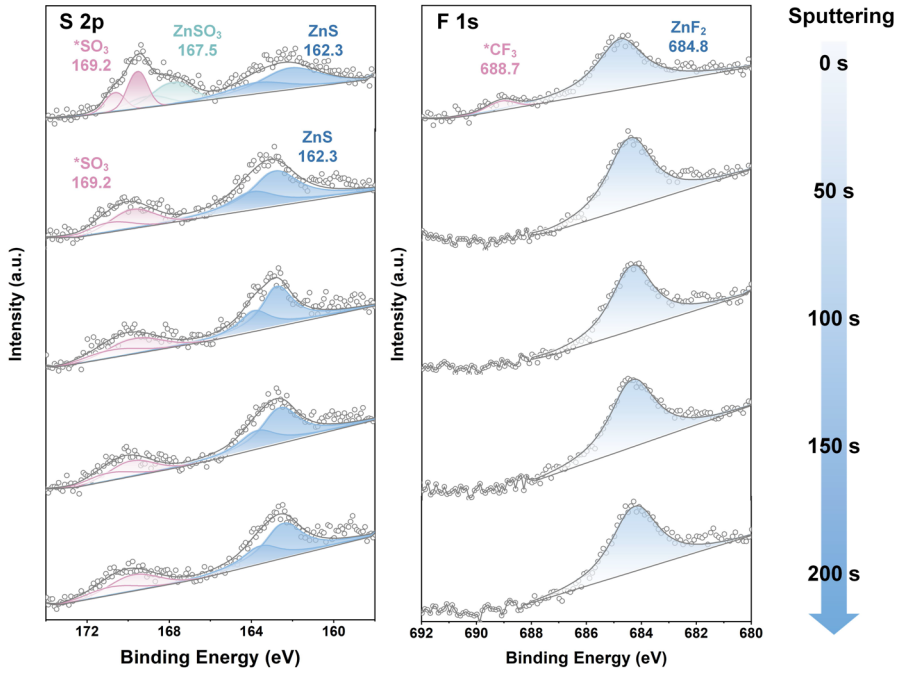

Fig. S30 XPS spectra of S 2p and F 1s for Zn cycled in 60%G2 electrolyte.

Ar^+ sputtering for 0s, 50s, 100s, 150s, and 200s was conducted to generate depth profiles. Zn anode samples were obtained from Zn//Zn symmetric cells with 60%G2 electrolyte after 20 cycles of stripping/plating (1 mA cm^{-2}, 1 mAh cm^{-2}).

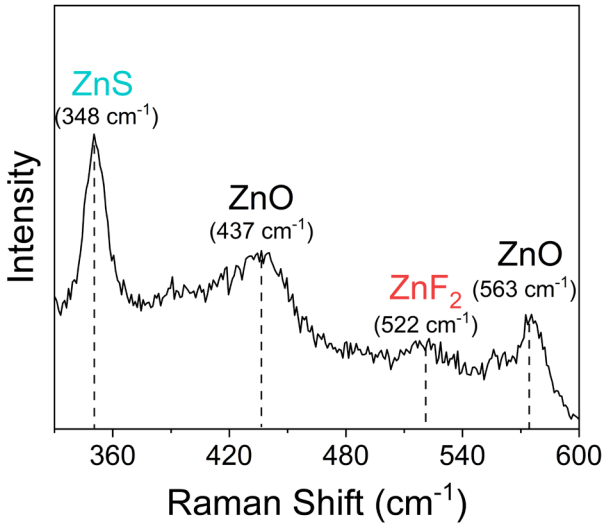

Fig. S31 Raman spectrum of Zn electrode after 20 stripping/plating cycles in the 60%G2 electrolyte.

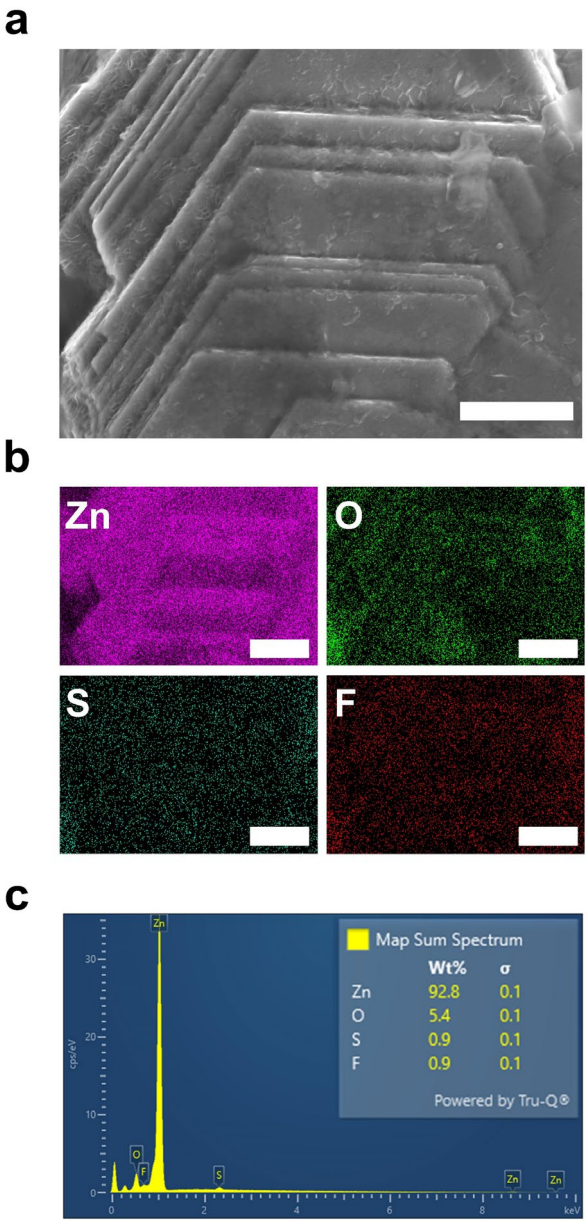

Fig. S32 SEM images and EDS mapping of Zn electrode after 20 stripping/plating cycles in 60%G2 electrolyte.

(a) Secondary electron image, (b) elemental mapping of Zn, O, S, and F, (c) area EDS spectrum and weight percentage of various elements. (Bar=2 μm)

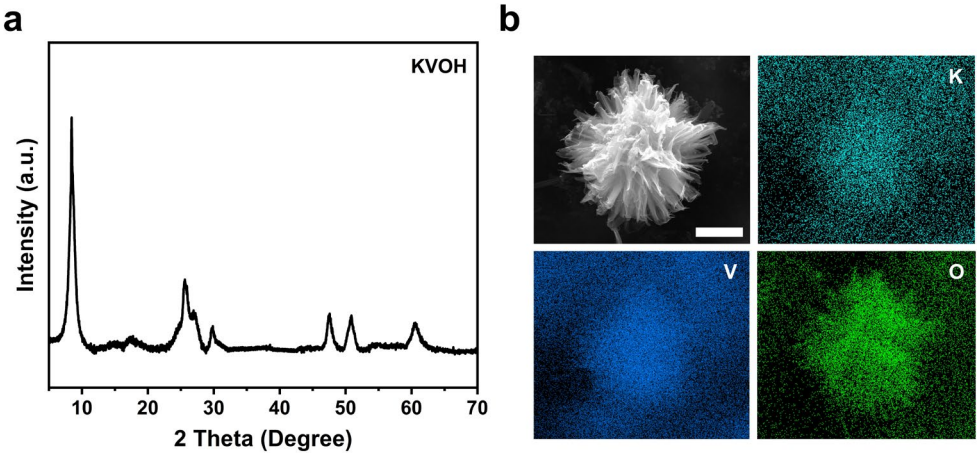

Fig. S33 Characterization of KVOH cathode material.

(a) XRD pattern, and (b) SEM image and elemental mapping analysis of KVOH (scale bar: 2 μm)

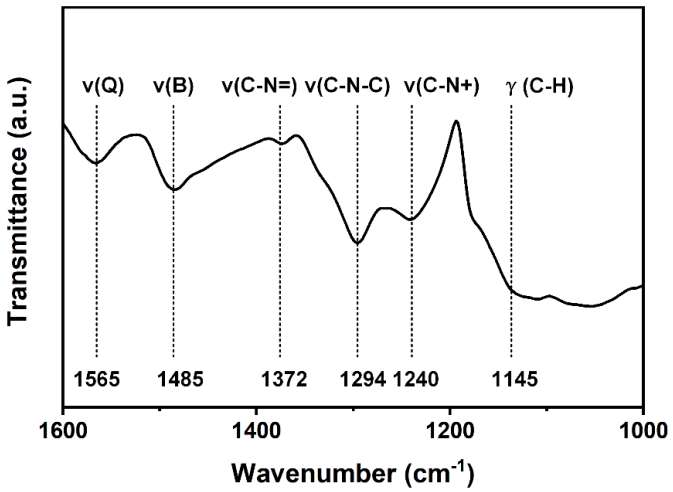

Fig. S34 Characterization of PANI cathode material.

FTIR spectrum of PANI and characteristic peak positions.

The peak at ~1565 cm^{-1} corresponds to the stretching vibration of quinoid rings (Q). The peak at ~1485 cm^{-1} corresponds to the stretching vibration of benzenoid rings (B). The peak at ~1372 cm^{-1} corresponds to the C–N= stretching vibration between benzenoid and quinoid units. [39] The peak at ~1294 cm^{-1} is ascribed to the π-electron delocalization induced in the polymer through protonation or C-N-C stretching vibration. The peak at ~1240 cm^{-1} is assigned to the C-N^+ stretching vibration in the polaron structure. [40, 41] The band at ~1145 cm^{-1} is due to the plane-bending vibration of C–H (modes of N=Q=N, Q=NH^+–B, and B–NH^+–B) formed during protonation. [42, 43]

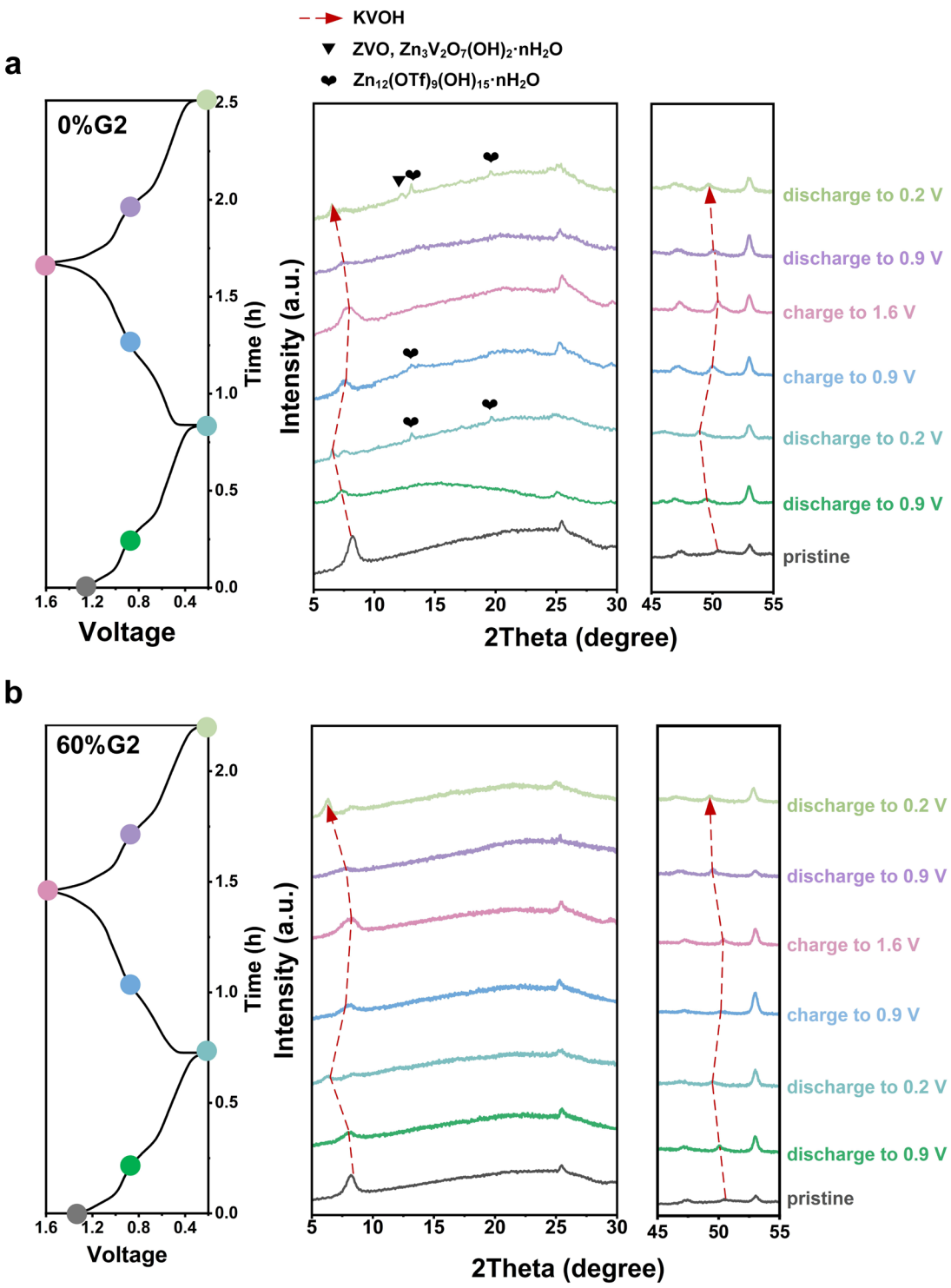

Fig. S35 *Ex-situ* XRD patterns of the KVOH cathode.

Ex-situ XRD patterns of the KVOH cathode in Zn//KVOH batteries with (a) 0%G2 and (b) 60%G2 electrolytes in various states at current density of 0.5 A g^{-1}.

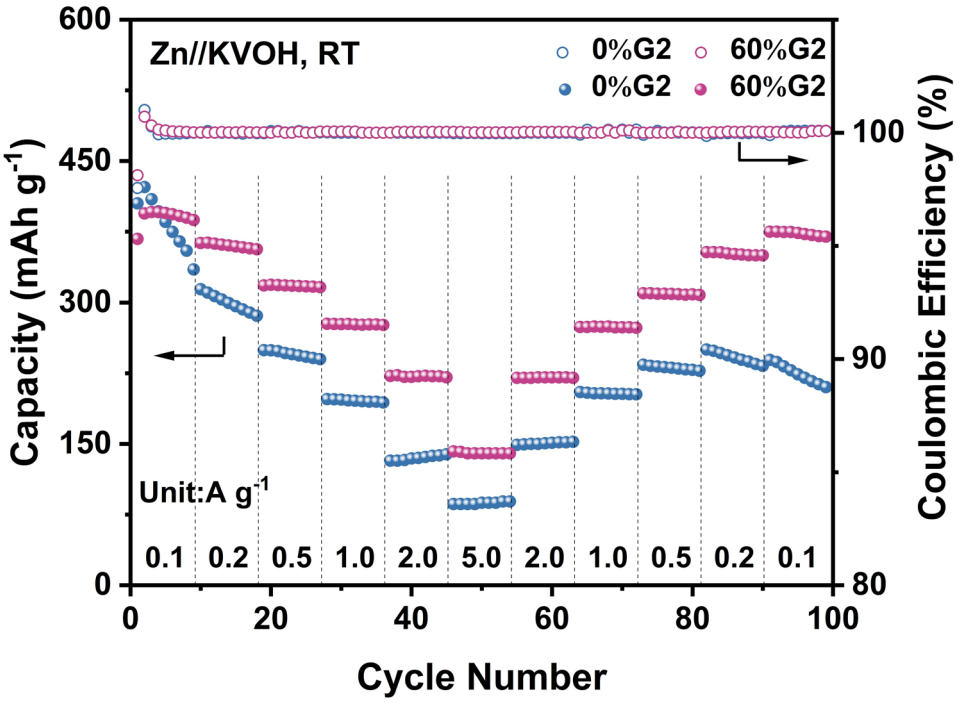

Fig. S36 Rate performance of Zn//KVOH batteries at RT.

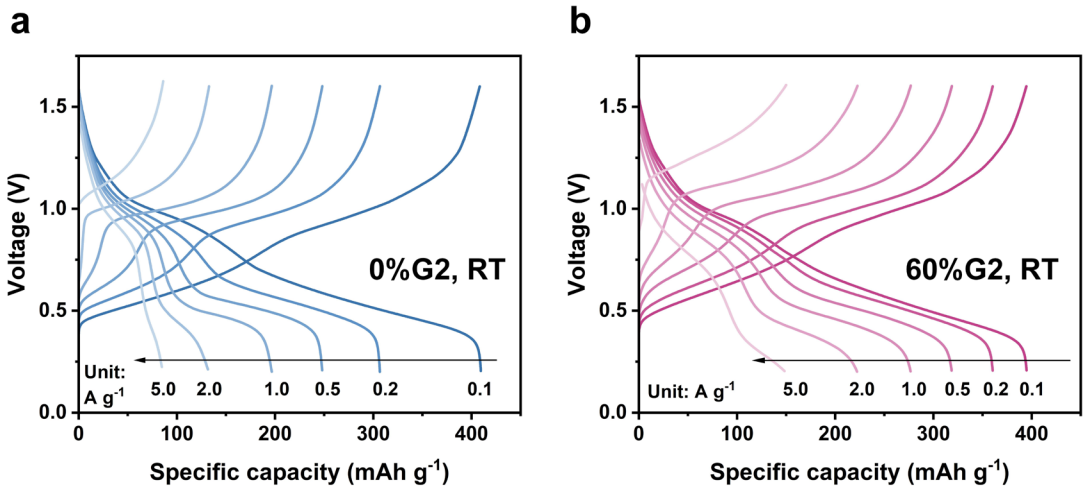

Fig. S37 Charge-discharge curves for Zn//KVOH batteries at RT.

Charge-discharge curves for Zn//KVOH cell (a) 0%G2 and (b) 60%G2 electrolyte at RT at current density of 0.1, 0.2, 0.5, 1.0, 2.0, and 5.0 A g^{-1}.

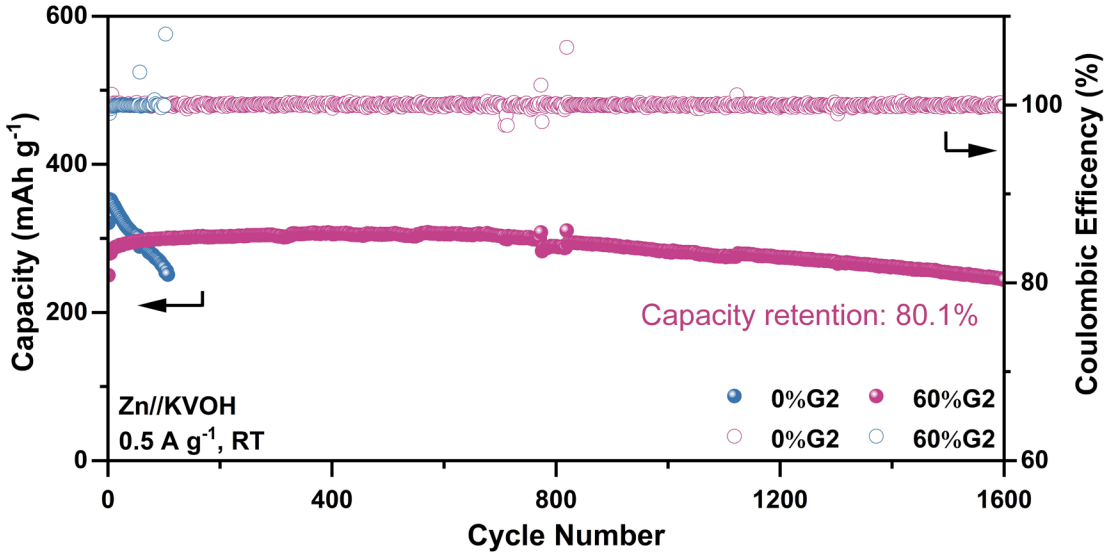

Fig. S38 Cycling performance of Zn//KVOH batteries at RT at 0.5 A g^{-1}.

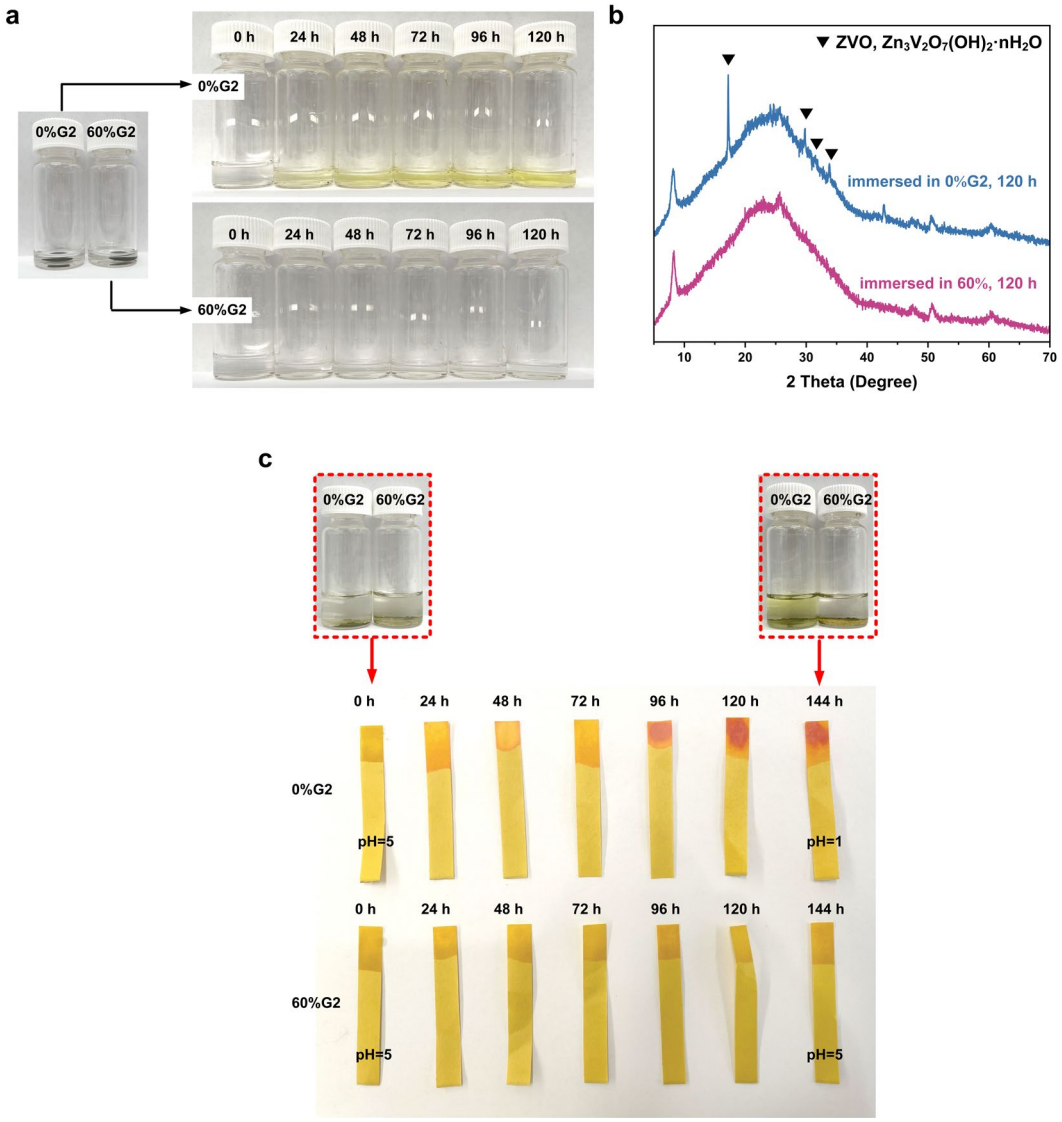

Fig. S39 The comparison of cathode dissolution in different electrolyte.

(a) Photographs of vials with 1 mL electrolyte (0%G2 and 60%G2), each with a piece of KVOH electrode immersed in it for 0 to 120 h. (b) XRD patterns of electrode immersed in 0%G2 and 60%G2 for 120 h. (c) pH of electrolytes (2 mL, 0%G2 or 60%G2) with KVOH (50 mg) from 0 h to 144 h and images of the electrolytes with KVOH at 0 and 144 h.

The decreased pH value in 0%G2 with electrode/cathode material is caused by the H^+ generated in the following two reactions: [44]

(1) Dissolution of KVOH: KVOH reacted with H_2O and formed $VO_2(OH)_2^-$ and H^+.

(2) Precipitation of ZVO: $VO_2(OH)_2^-$ from (1) reacted with Zn^{2+} and H_2O to form $Zn_3V_2O_7(OH)_2{\cdot}nH_2O$ and H^+.

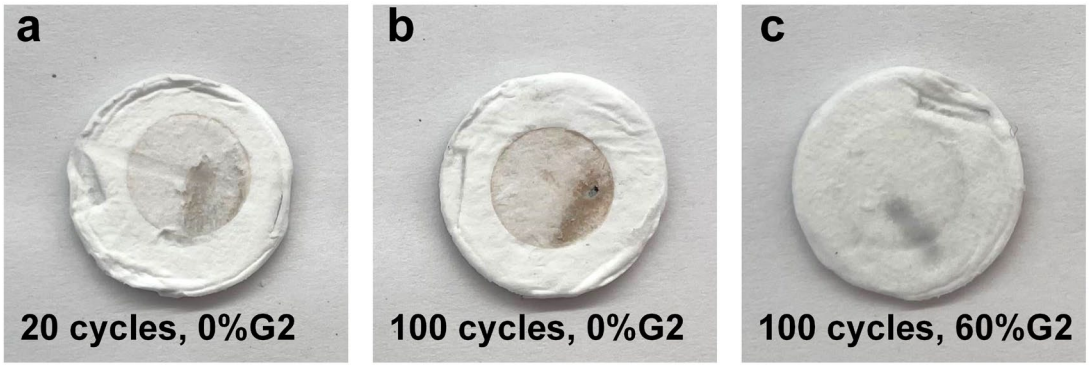

Fig. S40 Glass fiber separators in Zn//KVOH batteries.

Glass fiber separators in Zn//KVOH batteries after (a) 20 cycles in 0%G2 electrolyte, (b) 100 cycles in 0%G2 electrolyte, and (c) 100 cycles in 60%G2 electrolyte.

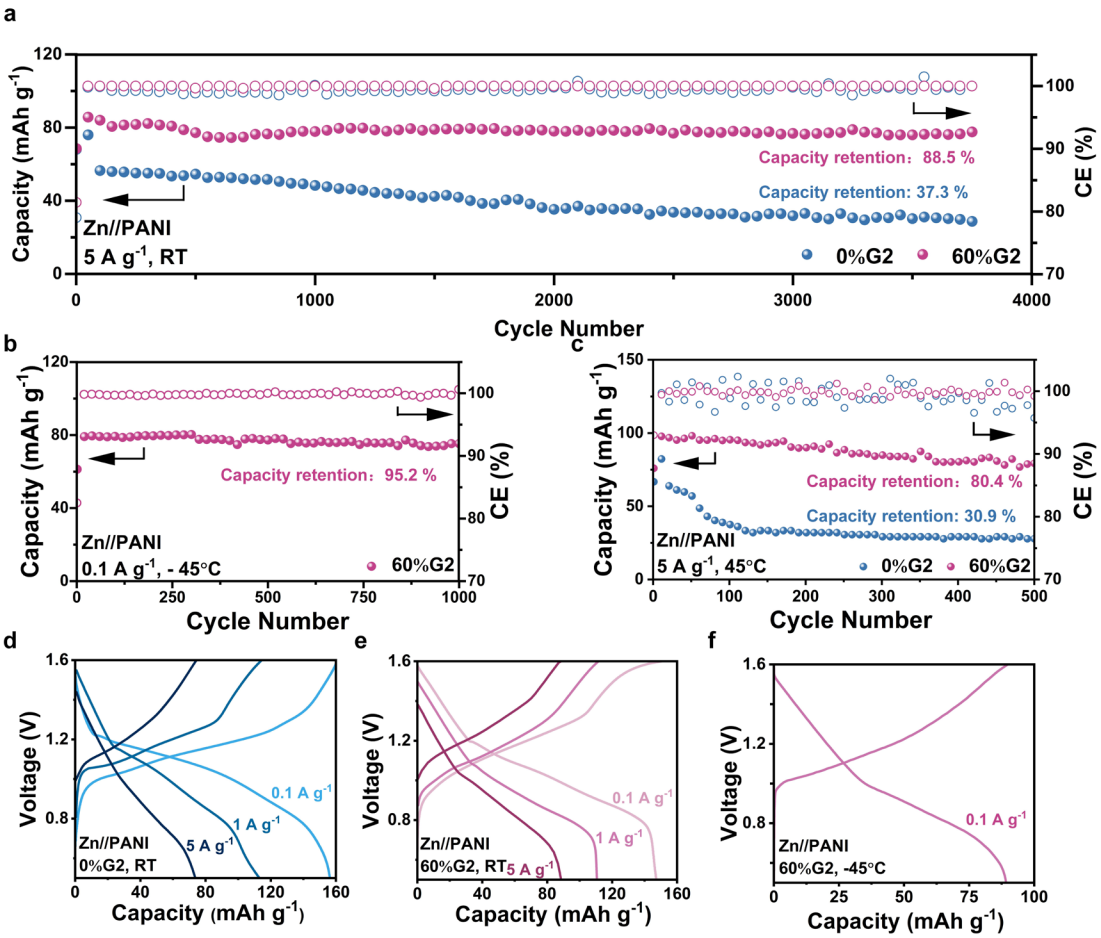

Fig. S41 Cycling performance of Zn//PANI batteries.

Cycling performance of Zn//PANI batteries with 0%G2 and 60%G2 electrolytes at (a) RT, (b) −45℃, (c) 45℃. Charge-discharge curves for Zn//PANI batteries with (d) 0%G2 electrolyte at RT, (e) 60%G2 electrolyte at RT, and (f) 60%G2 electrolyte at −45℃.

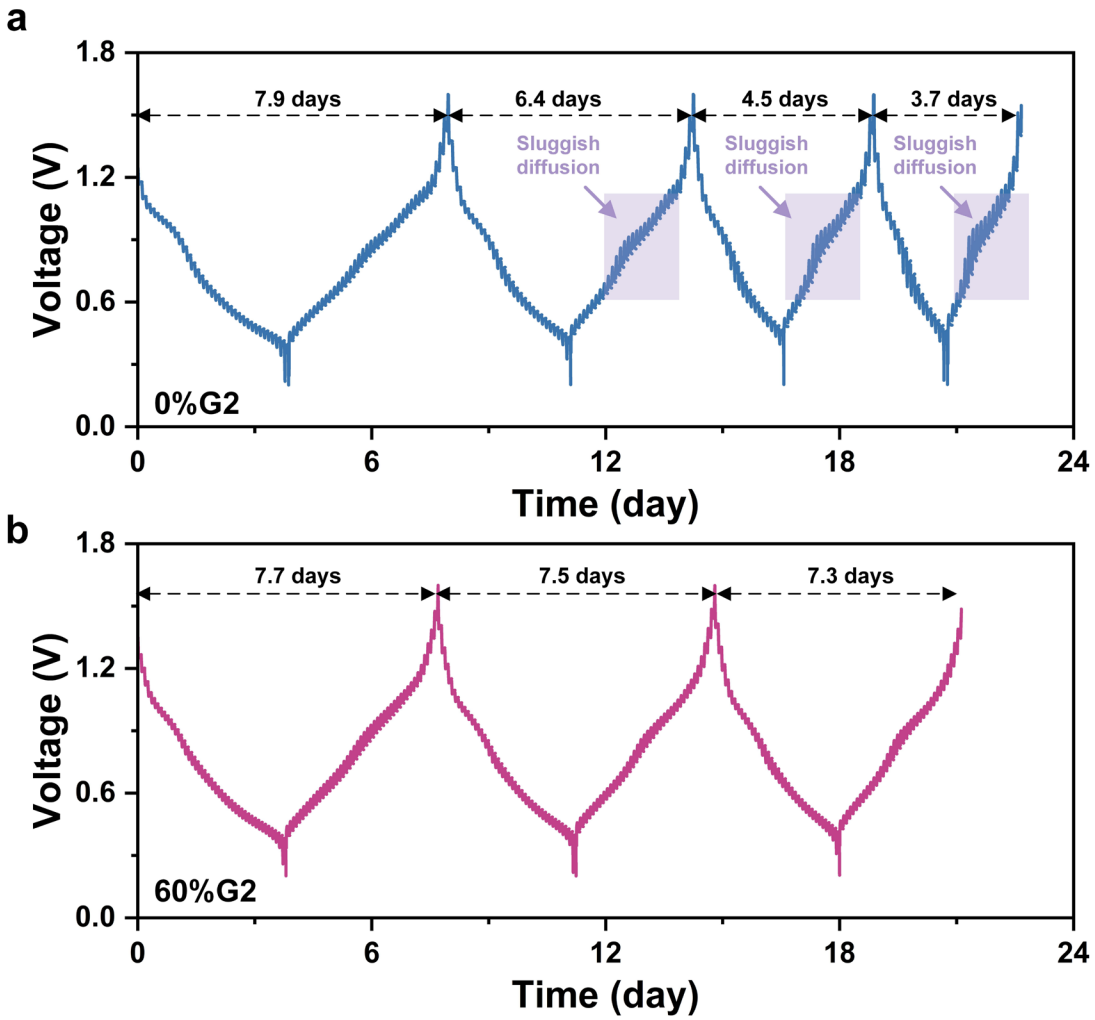

Fig. S42 GITT voltage profiles of KVOH.

GITT voltage profiles of KVOH in (a) 0%G2 and (b) 60%G2 electrolytes with a 100 mA g^{-1} pulsed current, 0.5 h pulse time, and a relaxation period of 2 h for each pulse.

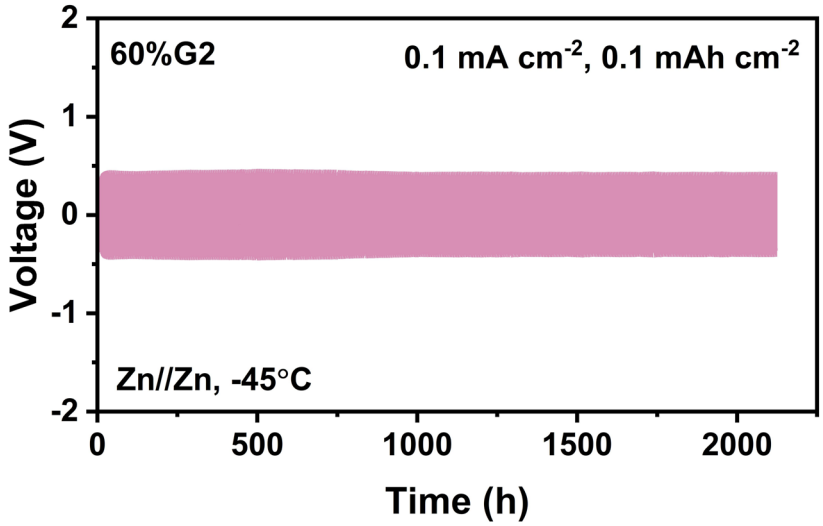

Fig. S43 Cycling performance of Zn//Zn symmetric cells at −45°C.

Voltage profiles of galvanostatic plating/stripping of Zn//Zn symmetric cells with 60%G2 electrolyte at 0.1 mA cm^{-2}, 0.1 mAh cm^{-2} at −45°C.

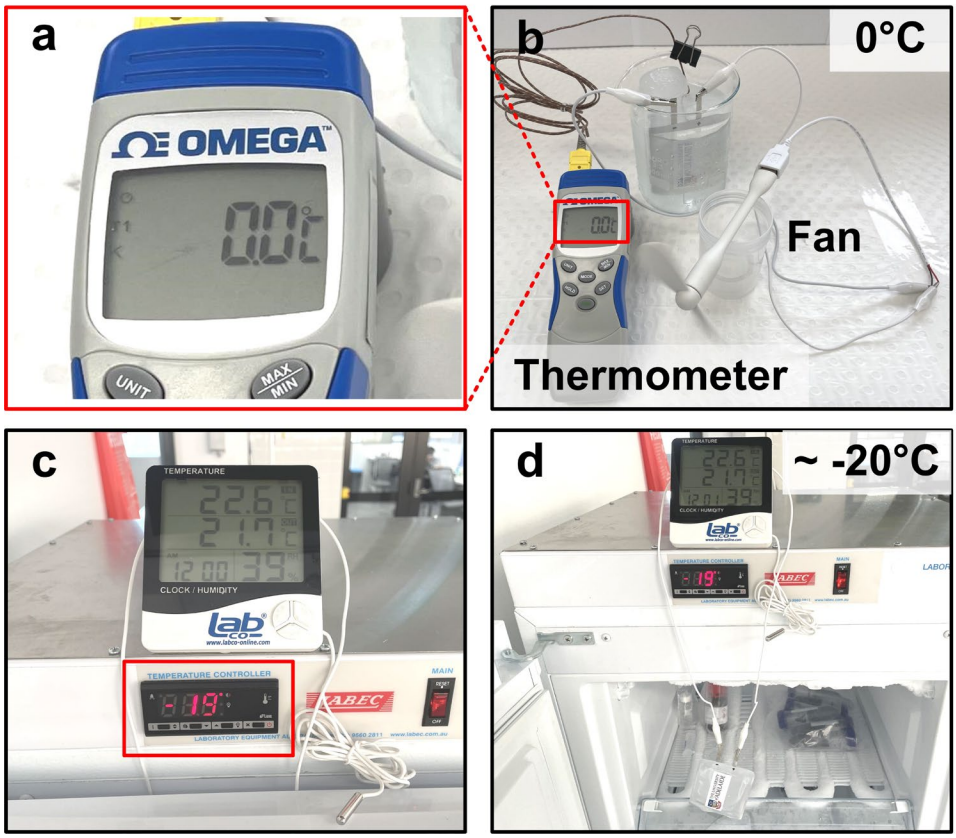

Fig. S44 Photos of devices powered by a Zn//KVOH pouch cell with 60%G2 electrolyte.

(a, b) Fan powered by a Zn//KVOH pouch cell at 0℃. (c, d) Thermometer powered by a Zn//KVOH pouch cell at ~ −20℃.

Ref.

1. M. Tian, C. Liu, J. Zheng, X. Jia, E. P. Jahrman, G. T. Seidler, D. Long, M. Atif, M. Alsalhi and G. Cao, *Energy Storage Materials*, 2020, **29**, 9-16.
2. F. Wan, L. Zhang, X. Wang, S. Bi, Z. Niu and J. Chen, *Adv. Funct. Mater.*, 2018, **28**, 1804975.
3. S. Liu, J. P. Vongsvivut, Y. Wang, R. Zhang, F. Yang, S. Zhang, K. Davey, J. Mao and Z. Guo, *Angew. Chem. Int. Ed.*, 2022, **62**, e202215600.
4. Z. Wang, F. Qi, L. Yin, Y. Shi, C. Sun, B. An, H. M. Cheng and F. Li, *Adv. Energy Mater.*, 2020, **10**, 1903843.
5. S. Liu, J. Mao, W. K. Pang, J. Vongsvivut, X. Zeng, L. Thomsen, Y. Wang, J. Liu, D. Li and Z. Guo, *Adv. Funct. Mater.*, 2021, **31**, 2104281.
6. J. Wang, R. M. Wolf, J. W. Caldwell, P. A. Kollman and D. A. Case, *J. Comput. Chem.*, 2004, **25**, 1157-1174.
7. Alan W Sousa da Silva and W. F. Vranken, *BMC Res. Notes*, 2012, **5**, 367.
8. G. Kresse av and J. F. b, *Comput. Mater. Sci.*, 1996, **6**, 15-50.
9. G. Kresse and J. Furthmuller, *Phys. Rev. B*, 1996, **54**, 11169-11186.
10. P. E. Blochl, *Phys. Rev. B: Condens. Matter Mater. Phys.*, 1994, **50**, 17953-17979.
11. G. Kresse and D. Joubert, *Phys. Rev. B*, 1999, **59**, 1758-1775.
12. John P. Perdew, Kieron Burke and M. Ernzerhof, *Phys. Rev. Lett.*, 1996, **77**, 3865-3868.
13. S. Grimme, J. Antony, S. Ehrlich and H. Krieg, *J. Chem. Phys.*, 2010, **132**, 154104.
14. W. M. Haynes, *CRC handbook of chemistry and physics*, CRC press, 2014.
15. C. Hu, G. Guo, H. Li, J. Wang, Z. Liu, L. Zheng and H. Zhang, *Surf. Interfaces*, 2023, **42**, 103421.
16. B. Xie, Q. Hu, X. Liao, X. Zhang, H. Lang, R. Zhao, Q. Zheng, Y. Huo, J. Zhao, D. Lin and X. L. Wu, *Adv. Funct. Mater.*, 2023, **34**, 2311961.
17. Y. Yang, G. Qu, H. Wei, Z. Wei, C. Liu, Y. Lin, X. Li, C. Han, C. Zhi and H. Li, *Adv. Energy Mater.*, 2023, **13**, 2203729.
18. H. Du, K. Wang, T. Sun, J. Shi, X. Zhou, W. Cai and Z. Tao, *Chem. Eng. J.*, 2022, **427**, 131705.
19. F. Ming, Y. Zhu, G. Huang, A. H. Emwas, H. Liang, Y. Cui and H. N. Alshareef, *J. Am. Chem. Soc.*, 2022, **144**, 7160-7170.
20. L. Liu, H. Lu, C. Han, X. Chen, S. Liu, J. Zhang, X. Chen, X. Wang, R. Wang, J. Xu, H. K. Liu, S. X. Dou and W. Li, *ACS Nano*, 2023, **17**, 23065-23078.
21. X. Cao, W. Xu, D. Zheng, F. Wang, Y. Wang, X. Shi and X. Lu, *Angew. Chem. Int. Ed.*, 2023, **63**, e202317302.
22. N. Chang, T. Li, R. Li, S. Wang, Y. Yin, H. Zhang and X. Li, *Energy Environ. Sci.*, 2020, **13**, 3527-3535.
23. L. Cao, D. Li, E. Hu, J. Xu, T. Deng, L. Ma, Y. Wang, X. Q. Yang and C. Wang, *J. Am. Chem. Soc.*, 2020, **142**, 21404-21409.
24. Q. Ma, R. Gao, Y. Liu, H. Dou, Y. Zheng, T. Or, L. Yang, Q. Li, Q. Cu, R. Feng, Z. Zhang, Y. Nie, B. Ren, D. Luo, X. Wang, A. Yu and Z. Chen, *Adv. Mater.*, 2022, **34**, e2207344.
25. Y. Ma, Q. Zhang, L. Liu, Y. Li, H. Li, Z. Yan and J. Chen, *Natl. Sci. Rev.*, 2022, **9**, nwac051.

26. Y. Qiu, X. Zheng, R. Zhang, Q. Lin, M. Li, J. Luo, S. Yang, Z. Liu, Q. Wang, Y. Yu and C. Yang, *Adv. Funct. Mater.*, 2023, **34**, 2310825.
27. Z. Li, Y. Liao, Y. Wang, J. Cong, H. Ji, Z. Huang and Y. Huang, *Energy Storage Materials*, 2023, **56**, 174-182.
28. D. Feng, F. Cao, L. Hou, T. Li, Y. Jiao and P. Wu, *Small*, 2021, **17**, e2103195.
29. X. Shi, J. Xie, J. Wang, S. Xie, Z. Yang and X. Lu, *Nat. Commun.*, 2024, **15**, 302.
30. N. Nikolić, V. Maksimović, G. Branković, P. Živković and M. Pavlović, *Zast. Mater.*, 2018, **59**, 256-264.
31. H. Zhang, Y. Zhong, J. Li, Y. Liao, J. Zeng, Y. Shen, L. Yuan, Z. Li and Y. Huang, *Adv. Energy Mater.*, 2022, **13**, 2203254.
32. N. Wang, Y. Yang, X. Qiu, X. Dong, Y. Wang and Y. Xia, *ChemSusChem*, 2020, **13**, 5556-5564.
33. T. Wei, Y. Peng, L. e. Mo, S. Chen, R. Ghadari, Z. Li and L. Hu, *Sci. China Mater.*, 2021, **65**, 1156-1164.
34. J. Hao, L. Yuan, C. Ye, D. Chao, K. Davey, Z. Guo and S. Qiao, *Angew. Chem., Int. Ed.*, 2020, **133**, 7442-7451.
35. A. Wang, W. Zhou, A. Huang, M. Chen, Q. Tian and J. Chen, *J Colloid Interface Sci*, 2021, **586**, 362-370.
36. J. Wang, Q. Zhu, F. Li, J. Chen, H. Yuan, Y. Li, P. Hu, M. S. Kurbanov and H. Wang, *Chem. Eng. J.*, 2022, **433**, 134589.
37. D. S. Liu, Y. Zhang, S. Liu, L. Wei, S. You, D. Chen, M. Ye, Y. Yang, X. Rui, Y. Qin and C. C. Li, *Adv. Funct. Mater.*, 2022, **32**, 2111714.
38. W. Huang, R. Freeh and R. A. Wheeler, *J. Phys. Chem.*, 1994, **98**, 100-110.
39. Y. Wei, K. F. Hsueh and G. W. Jang, *Macromolecules* 1994, **27**, 518–525.
40. T. Abdiryim, R. Jamal and I. Nurulla, *J. Appl. Polym. Sci.*, 2007, **105**, 576-584.
41. T. Abdiryim, Z. Xiao-Gang and R. Jamal, *Mater. Chem. Phys.*, 2005, **90**, 367-372.
42. Y. He, *Appl. Surf. Sci.*, 2005, **249**, 1-6.
43. W. Shao, R. Jamal, F. Xu, A. Ubul and T. Abdiryim, *Materials*, 2012, **5**, 1811-1825.
44. Y. Kim, Y. Park, M. Kim, J. Lee, K. J. Kim and J. W. Choi, *Nat. Commun.*, 2022, **13**, 2371.